LETTER

https://doi.org/10.1038/s41586-019-0948-2

Sleep modulates haematopoiesis and protects against atherosclerosis

Cameron S. McAlpine[1], Máté G. Kiss[1,2,3], Sara Rattik[1], Shun He[1], Anne Vassalli[4], Colin Valet[1], Atsushi Anzai[1], Christopher T. Chan[1], John E. Mindur[1], Florian Kahles[1], Wolfram C. Poller[1], Vanessa Frodermann[1], Ashley M. Fenn[1], Annemijn F. Gregory[1], Lennard Halle[1], Yoshiko Iwamoto[1], Friedrich F. Hoyer[1], Christoph J. Binder[2,3], Peter Libby[5], Mehdi Tafti[4], Thomas E. Scammell[6], Matthias Nahrendorf[1,7] & Filip K. Swirski[1,7]*

Sleep is integral to life[1]. Although insufficient or disrupted sleep increases the risk of multiple pathological conditions, including cardiovascular disease[2], we know little about the cellular and molecular mechanisms by which sleep maintains cardiovascular health. Here we report that sleep regulates haematopoiesis and protects against atherosclerosis in mice. We show that mice subjected to sleep fragmentation produce more Ly-6C^{high} monocytes, develop larger atherosclerotic lesions and produce less hypocretin—a stimulatory and wake-promoting neuropeptide—in the lateral hypothalamus. Hypocretin controls myelopoiesis by restricting the production of CSF1 by hypocretin-receptor-expressing pre-neutrophils in the bone marrow. Whereas hypocretin-null and haematopoietic hypocretin-receptor-null mice develop monocytosis and accelerated atherosclerosis, sleep-fragmented mice with either haematopoietic CSF1 deficiency or hypocretin supplementation have reduced numbers of circulating monocytes and smaller atherosclerotic lesions. Together, these results identify a neuro-immune axis that links sleep to haematopoiesis and atherosclerosis.

Poor or insufficient sleep is an increasingly important public health issue[3], as nearly half of adults in the United States sleep fewer than the recommended seven to eight hours per day[4]. Lack of sleep increases risk of obesity[5], diabetes[6], cancer[7] and cardiovascular disease[2], but we know little about the underlying mechanisms that link sleep to disease.

To investigate how sleep might protect against cardiovascular disease, we subjected atherosclerosis-prone *Apoe*$^{-/-}$ mice to chronic sleep fragmentation (SF)[8] (Extended Data Fig. 1a and Supplementary Video 1). We found no changes in body weight, plasma cholesterol or glucose tolerance (Extended Data Fig. 1b–e); however, mice developed progressively larger atherosclerotic lesions compared to controls (Fig. 1a and Extended Data Fig. 1f–h). Not only did lesion volume increase in SF mice (Fig. 1b), but aortas from SF mice contained more Ly-6C^{high} monocytes, neutrophils and macrophages (Fig. 1c); a change that did not result from increased proliferation of aortic macrophages (Extended Data Fig. 1i).

Leukocytosis is predictive of cardiovascular disease[9]. Although myeloid cell numbers in the blood of mice fluctuated according to a circadian pattern with a peak at zeitgeber time (ZT)5 and a nadir at ZT14 (Fig. 1d), mice subjected to sleep fragmentation had significantly more circulating Ly-6C^{high} monocytes and neutrophils during the light period. Rhythmicity analysis revealed that the circadian amplitude was increased ($0.7 \pm 0.16 \times 10^5$ compared to $1.5 \pm 0.15 \times 10^5$, in control and SF mice, respectively, $P = 0.02$, for Ly-6C^{high} monocytes and $3.6 \pm 0.17 \times 10^5$ compared to $5.1 \pm 0.11 \times 10^5$, in control and SF mice, respectively, $P = 0.13$, for neutrophils), but the period and phase were unaltered. Sleep fragmentation did not change lymphocyte numbers (Extended Data Fig. 1j–l). To understand the influence of sleep on circadian leukocyte migration to tissues[10,11], we profiled leukocytes in various organs at ZT3 and ZT14. Both control and SF mice had elevated Ly-6C^{high} monocyte and neutrophil levels in various tissues during the dark period, and these increases were higher in SF mice (Extended Data Fig. 2). These observations align with human studies that have linked sleep curtailment or interruption with leukocyte numbers[12,13].

Next, we focused on haematopoiesis. In *Apoe*$^{-/-}$ mice, sleep fragmentation increased proliferation of lineage (Lin)$^-$Kit$^+$Sca1$^+$ (LSK) haematopoietic progenitors in the bone marrow, and this increase corresponded to an approximately twofold-higher number of bone marrow LSK cells (Fig. 1e) and other progenitor subsets (Extended Data Fig. 3a). The spleens of SF mice contained more LSK cells and granulocyte–macrophage progenitors, which indicates heightened extramedullary haematopoiesis (Extended Data Fig. 3b). Sleep fragmentation promoted myelopoiesis not only in *Apoe*$^{-/-}$ mice that were fed a high-fat diet, but also in C57BL/6 mice fed a chow diet (Extended Data Fig. 3c). Together, these data show that sleep fragmentation boosts myeloid-biased haematopoiesis.

Mice subjected to sleep fragmentation had normal bone structure (Extended Data Fig. 4a, b) and leukocytosis persisted even after prolonged treatment with antibiotics (Extended Data Fig. 4c), suggesting that enhanced myelopoiesis was not driven by either physical alterations to the bone or the microbiome, respectively. Because stress activates the sympathetic nervous system, which can heighten haematopoiesis[14], we wondered whether sleep-fragmentation-induced myelopoiesis similarly depended on activation of the sympathetic nervous system, but found no evidence for such a mechanism (Extended Data Fig. 5a–d). Nevertheless, SF mice were more anxious (Extended Data Fig. 5e–g), which demonstrates that mice do not easily habituate to sleep fragmentation.

We then focused on the hypothalamus and, specifically, on expression of transcripts that encode sleep-regulating proteins (Extended Data Fig. 5h–j). Sleep fragmentation decreased expression of hypocretin (*Hcrt*, also known as orexin) in the hypothalamus (Fig. 1f–h), correlating with reduced levels of the isoform hypocretin-1 in plasma and bone marrow (Fig. 1i). Hypothalamic hypocretin reduced gradually and correlated inversely with leukocytosis (Extended Data Fig. 6a). We did not see alterations in dynorphin, a co-transmitter of hypocretin[15] (Extended Data Fig. 6b–e) or any evidence for death of hypocretin-producing neurons (Extended Data Fig. 6f), which suggests that specific repression of hypocretin occurred, potentially mediated by neuropeptide Y[16] (Extended Data Fig. 5h). Furthermore, sleep recovery following sleep fragmentation restored hypothalamic hypocretin content and normalized myelopoiesis (Extended Data Fig. 6g–i). These data intrigued us, because hypocretin mediates metabolism, sleep and appetite[17], and autoimmune destruction of hypocretin neurons causes

[1]Center for Systems Biology, Massachusetts General Hospital and Harvard Medical School, Boston, MA, USA. [2]Department of Laboratory Medicine, Medical University of Vienna, Vienna, Austria. [3]CeMM Research Center for Molecular Medicine of the Austrian Academy of Sciences, Vienna, Austria. [4]Department of Physiology, Faculty of Biology and Medicine, University of Lausanne, Lausanne, Switzerland. [5]Cardiovascular Division, Department of Medicine, Brigham and Women's Hospital, Boston, MA, USA. [6]Department of Neurology, Beth Israel Deaconess Medical Center, Boston, MA, USA. [7]Department of Radiology, Massachusetts General Hospital and Harvard Medical School, Boston, MA, USA. *e-mail: fswirski@mgh.harvard.edu

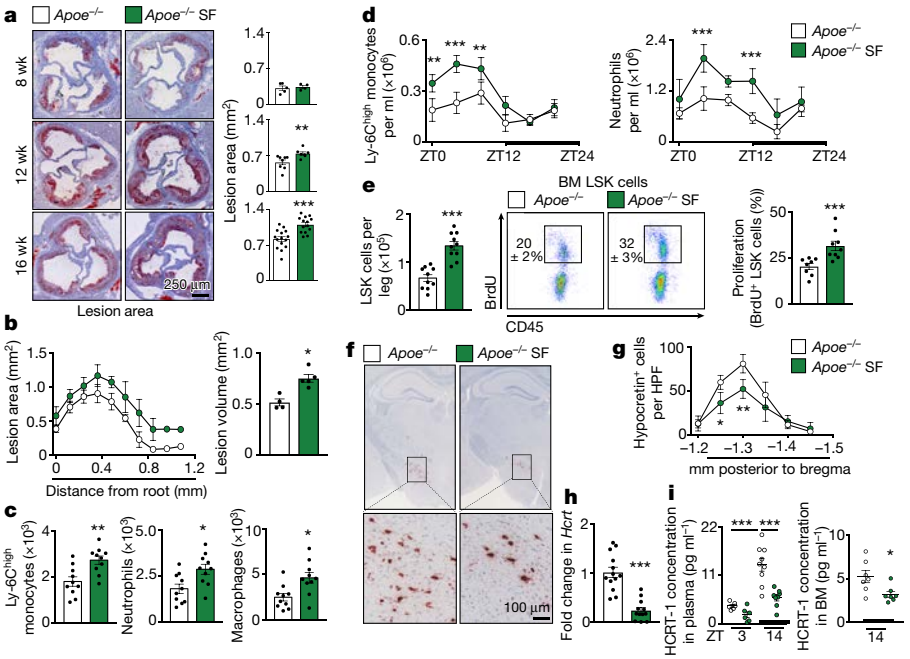

Fig. 1 | Sleep fragmentation aggravates atherosclerosis, increases haematopoiesis and decreases production of hypocretin in the hypothalamus. Assessment of sleep fragmentation in *Apoe*$^{-/-}$ mice fed a high-fat diet. **a**, Cross-sections of aortic roots stained with oil red O and quantification of atherosclerotic lesion areas after varying lengths of sleep fragmentation ($n = 5$ *Apoe*$^{-/-}$ mice after 8 weeks of control sleep; $n = 4$ *Apoe*$^{-/-}$ SF mice after 8 weeks of sleep fragmentation; $n = 8$ *Apoe*$^{-/-}$ mice after 12 weeks of control sleep; $n = 7$ *Apoe*$^{-/-}$ SF mice after 12 weeks of sleep fragmentation; $n = 15$ *Apoe*$^{-/-}$ mice after 16 weeks of control sleep; $n = 14$ *Apoe*$^{-/-}$ SF mice after 16 weeks of sleep fragmentation). **b**, Measurement of lesion volume after 16 weeks of sleep fragmentation ($n = 4$ *Apoe*$^{-/-}$ mice; $n = 5$ *Apoe*$^{-/-}$ SF mice). **c**, Quantification using flow cytometry of neutrophils, macrophages and Ly-6C^{high} monocytes in the aorta of *Apoe*$^{-/-}$ mice and *Apoe*$^{-/-}$ SF mice after 16 weeks of sleep fragmentation ($n = 10$ mice per group). **d**, Quantification of circulating Ly-6C^{high} monocytes and neutrophils over 24 h after 16 weeks of sleep fragmentation (ZT0, lights on; ZT12, lights off; $n = 4$ per group). $^{**}P < 0.01$, $^{***}P < 0.001$, two-way analysis of variance (ANOVA). **e**, Quantification of bone marrow LSK cells and BrdU incorporation after 16 weeks of sleep fragmentation (for LSK cells per leg, $n = 10$ mice per group; for proliferation assays, $n = 8$ *Apoe*$^{-/-}$ mice and $n = 9$ *Apoe*$^{-/-}$ SF mice). **f**, Immunohistochemistry images stained for hypocretin in the hypothalamus after 16 weeks of sleep fragmentation. **g**, Quantification of hypocretin^{+} cells per high-power field (HPF) in the hypothalamus after 16 weeks of sleep fragmentation ($n = 4$ *Apoe*$^{-/-}$ mice; $n = 5$ *Apoe*$^{-/-}$ SF mice, of two independent experiments). $^{**}P < 0.01$, two-way ANOVA. **h**, Transcript expression of hypocretin in the hypothalamus after 16 weeks of sleep fragmentation ($n = 12$ mice per group). **i**, Measurement of hypocretin-1 (HCRT-1) protein in plasma and bone marrow fluid after 16 weeks of sleep fragmentation ($n = 6$ mice per group for plasma at ZT3; $n = 9$ *Apoe*$^{-/-}$ mice for plasma at ZT14; $n = 8$ *Apoe*$^{-/-}$ SF mice for plasma at ZT14; $n = 7$ mice per group for bone marrow at ZT14). $^{***}P < 0.001$, one-way ANOVA. Data are mean ± s.e.m., $^{*}P < 0.05$, $^{**}P < 0.01$, $^{***}P < 0.001$, two-tailed Mann–Whitney *U*-tests unless otherwise indicated.

narcolepsy[18] and a pro-inflammatory immune signature[19]. In keeping with the function of hypocretin in the promotion of appetite, SF mice consumed less food than controls (Extended Data Fig. 5k).

In humans, reduced plasma hypocretin is associated with risk of myocardial infarction[20], heart failure[21] and obesity[22]. Similarly, studies suggest that patients with narcolepsy have heightened risk of heart disease[23]. In mice, deleting hypocretin severely fragments sleep–wake cycles, causes cataplexy and promotes diet-induced obesity[24,25]. Moreover, deleting the hypocretin receptor-2 worsens healing after myocardial infarction[21]. We therefore profiled leukocytes in hypocretin-null (*Hcrt*$^{-/-}$) mice and found a higher number of Ly-6C^{high} monocytes and neutrophils in the blood, spleen and bone marrow relative to wild-type controls (Fig. 2a, b and Extended Data Fig. 7). Rhythmicity analysis of *Hcrt*$^{-/-}$ mouse blood revealed that Ly-6C^{high} monocytes and neutrophils had elevated circadian amplitudes ($1.8 \pm 0.32 \times 10^5$ compared to $3.7 \pm 0.55 \times 10^5$, in wild-type and *Hcrt*$^{-/-}$ mice, respectively, $P = 0.02$, for Ly-6C^{high} monocytes and $4.1 \pm 0.69 \times 10^5$ compared to $8.1 \pm 0.11 \times 10^5$, in wild-type and *Hcrt*$^{-/-}$ mice, respectively, $P = 0.03$, for neutrophils), but that the period and phase were unchanged. Bone marrow from *Hcrt*$^{-/-}$ mice had more haematopoietic progenitors along with increased proliferation of LSK cells (Fig. 2c and Extended Data Fig. 7). As in the SF mice, accelerated haematopoiesis in hypocretin-deficient mice did not appear to depend on the microbiome (Extended Data Fig. 4d). These results suggest that sleep regulates haematopoiesis through hypocretin.

Next, we tested whether hypocretin can affect haematopoiesis and atherosclerosis. We found that the hypothalamus produced nearly all of the hypocretin (Extended Data Fig. 8a, b). Sixteen weeks of sleep fragmentation did not alter hypocretin production in the bone and bone marrow (Extended Data Fig. 8c), which indicates that the hypothalamus was the relevant source affected by sleep. Indeed, we found substantial concentrations of the neuropeptide in the cerebrospinal fluid, plasma and bone marrow fluid of wild-type but not *Hcrt*$^{-/-}$ mice, and we detected high levels of HCRT-1 in the plasma and bone marrow fluid of *Hcrt*$^{-/-}$ mice after injecting HCRT-1 into the cerebrospinal fluid of the cisterna magna (Extended Data Fig. 8d, e). Consequently, we generated chimeric mice lacking hypocretin production in either the non-haematopoietic compartment (including the hypothalamus) or haematopoietic cells (Fig. 2d), and found heightened haematopoiesis in *Hcrt*$^{-/-}$ mice containing wild-type bone marrow cells (Fig. 2e). We also placed *Hcrt*$^{-/-}$ mice in parabiosis with wild-type mice (Fig. 2f), noting that wild-type-partnered *Hcrt*$^{-/-}$ mice had suppressed haematopoiesis compared to *Hcrt*$^{-/-}$-partnered *Hcrt*$^{-/-}$ mice (Fig. 2g). These data suggest that hypothalamus-produced hypocretin can enter the circulation to affect haematopoiesis in the distal bone marrow[26,27]. To determine whether hypocretin deficiency aggravates atherosclerosis, we generated *Hcrt*$^{-/-}$*Apoe*$^{-/-}$ mice, which had larger lesions with more aortic leukocytes than did *Apoe*$^{-/-}$ controls (Fig. 2h, i).

Having identified a link between hypocretin, haematopoiesis and atherosclerosis, we examined the underlying mechanism.

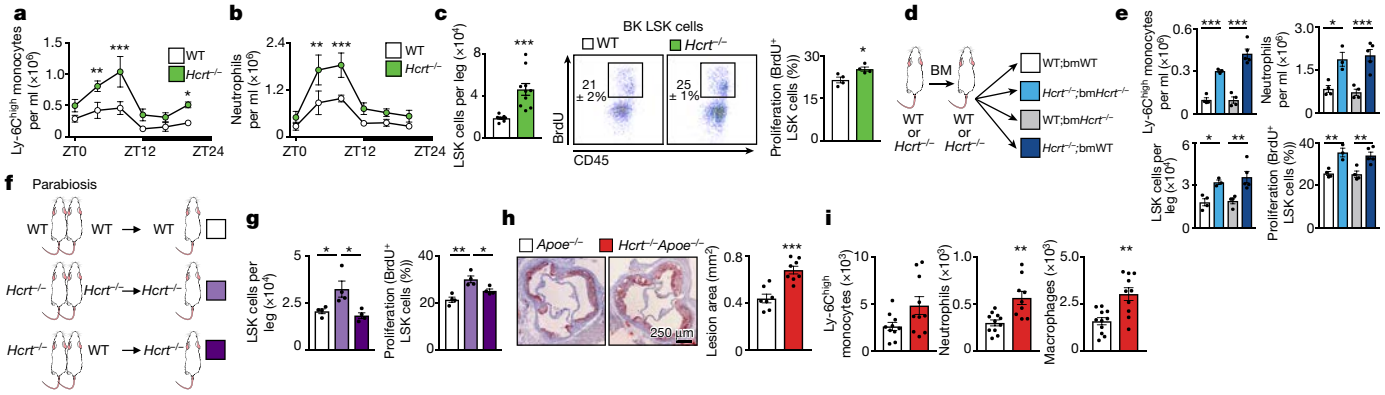

Fig. 2 | Hypocretin suppresses haematopoiesis and atherosclerosis. Assessment of haematopoiesis and atherosclerosis in *Hcrt*$^{-/-}$ mice. **a**, **b**, Quantification of Ly-6C^{high} monocytes (**a**) and neutrophils (**b**) in the blood of *Hcrt*$^{-/-}$ and wild-type mice over 24 h ($n = 3$ mice per group). $^{**}P < 0.01$, $^{***}P < 0.001$, two-way ANOVA. **c**, Quantification of bone marrow LSK cells and BrdU incorporation in wild-type and *Hcrt*$^{-/-}$ mice (for LSK cells per leg, $n = 8$ wild-type mice and $n = 10$ *Hcrt*$^{-/-}$ mice; for proliferation assays, $n = 4$ mice per group). **d**, Schematic of chimeric models. **e**, Assessment of blood Ly-6C^{high} monocytes and neutrophils, bone marrow LSK cells and BrdU incorporation in chimeric mice ($n = 4$ WT;bmWT mice; $n = 3$ *Hcrt*$^{-/-}$;bm*Hcrt*$^{-/-}$ mice; $n = 4$ WT;bm*Hcrt*$^{-/-}$ mice; $n = 5$ *Hcrt*$^{-/-}$;bmWT mice). $^{*}P < 0.05$, $^{**}P < 0.01$, $^{***}P < 0.001$, one-way ANOVA. **f**, Schematic of parabiosis models. **g**, Quantification of LSK cells and BrdU incorporation in the bone marrow of parabiosis mice ($n = 4$ per group). $^{*}P < 0.05$, $^{**}P < 0.01$, one-way ANOVA. **h**, Images of cross-sections of aortic roots stained with oil red O and quantification of atherosclerotic lesion areas in *Apoe*$^{-/-}$ mice and *Hcrt*$^{-/-}$*Apoe*$^{-/-}$ mice fed a high-fat diet for 16 weeks ($n = 7$ *Apoe*$^{-/-}$ mice; $n = 8$ *Hcrt*$^{-/-}$*Apoe*$^{-/-}$ mice). **i**, Aortic myeloid cells in *Apoe*$^{-/-}$ and *Hcrt*$^{-/-}$*Apoe*$^{-/-}$ mice (for Ly-6C^{high} monocytes, $n = 10$ mice per group; for neutrophils, $n = 11$ *Apoe*$^{-/-}$ mice and $n = 9$ *Hcrt*$^{-/-}$*Apoe*$^{-/-}$ mice; for macrophages, $n = 11$ *Apoe*$^{-/-}$ mice and $n = 10$ *Hcrt*$^{-/-}$*Apoe*$^{-/-}$ mice). Data are mean ± s.e.m., $^{*}P < 0.05$, $^{**}P < 0.01$, $^{***}P < 0.001$, two-tailed Mann–Whitney *U*-tests unless otherwise indicated.

Although hypocretin receptor-1 (*Hcrtr1*) and hypocretin receptor-2 (*Hcrtr2*) expression was the highest in the hypothalamus, we detected *Hcrtr1* in multiple tissues, including the bone marrow (Extended Data Fig. 8f, g). However, adding hypocretin to granulocyte–macrophage colony-forming cultures had no effect on haematopoiesis in vitro (Extended Data Fig. 8h). We therefore sorted 14 different cell types from the bone marrow and found that neutrophils—but not other cells—expressed *Hcrtr1* mRNA (Fig. 3a) and HCRTR1 protein (Extended Data Fig. 8i). We next sorted neutrophils by maturation stage[28] (Extended Data Fig. 9a) and found that pre-neutrophils expressed *Hcrtr1* most abundantly (Fig. 3b). Using knockout-reporter *Hcrtr1*$^{GFP/GFP}$ mice[29], we identified a subset of bone-marrow-resident

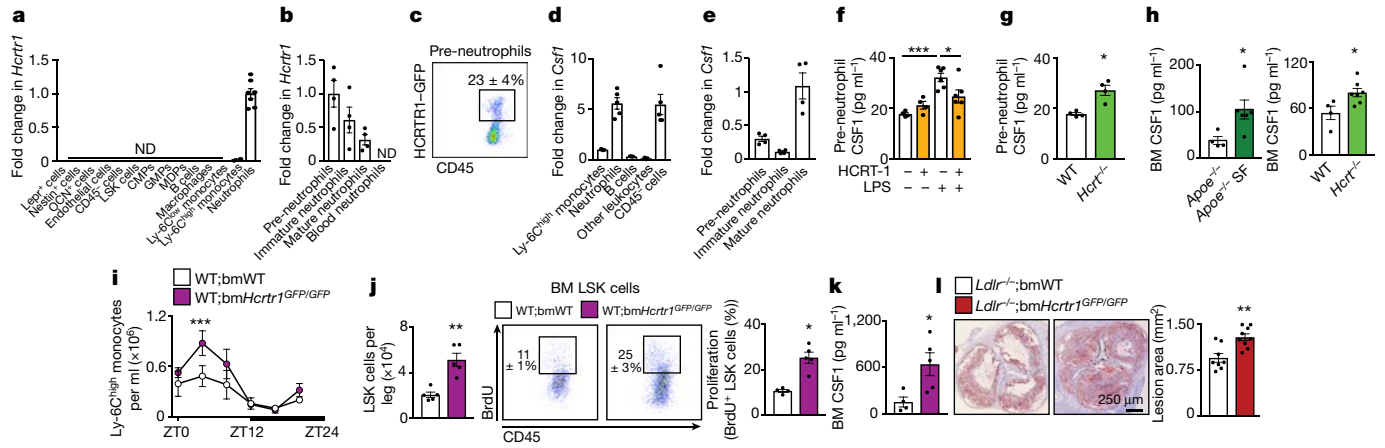

Fig. 3 | Hypocretin controls production of CSF1 by pre-neutrophils in the bone marrow. *Hcrtr1* mRNA in cells sorted from bone marrow ($n = 4$ mice except neutrophils, $n = 7$ mice). CMPs, common myeloid progenitors; GMPs, granulocyte–macrophage progenitors; MDPs, monocyte–dendritic cell progenitors. **b**, *Hcrtr1* mRNA expression in bone marrow and blood neutrophil populations ($n = 4$ mice). **c**, Flow cytometry plot of HCRTR1^{+} pre-neutrophils in the bone marrow of wild-type mice transplanted with *Hcrtr1*$^{GFP/GFP}$ bone marrow. **d**, *Csf1* expression in sorted bone marrow cells (for Ly-6C^{high} monocytes, B cells and other leukocytes, $n = 3$ mice; for neutrophils and CD45^{-} cells, $n = 5$ mice). **e**, *Csf1* expression in sorted bone marrow neutrophil populations ($n = 4$ mice). **f**, CSF1 production by pre-neutrophils sorted from wild-type mice and exposed to lipopolysaccharides (LPS) and/or HCRT-1 (for untreated and HCRT-1, $n = 4$ mice per group; for LPS, and LPS and HCRT-1, $n = 6$ mice per group). $^{*}P < 0.05$, $^{***}P < 0.001$, one-way ANOVA. **g**, CSF1 production by pre-neutrophils sorted from wild-type and *Hcrt*$^{-/-}$ mice ($n = 4$ mice per group). **h**, Concentration of CSF1 in the bone marrow of *Apoe*$^{-/-}$ SF mice and *Hcrt*$^{-/-}$ mice ($n = 4$ *Apoe*$^{-/-}$ mice; $n = 6$ *Apoe*$^{-/-}$ SF mice; $n = 4$ wild-type mice; $n = 7$ *Hcrt*$^{-/-}$ mice). **i**, Quantification of blood Ly-6C^{high} monocytes over 24 h in WT;bm*Hcrtr1*$^{GFP/GFP}$ mice ($n = 3$ per group). $^{***}P < 0.001$, two-way ANOVA. **j**, Quantification of bone marrow LSK cells and proliferation of LSK cells in wild-type mice transplanted with wild-type or *Hcrtr1*$^{GFP/GFP}$ bone marrow cells (for LSK cells per leg, $n = 5$ mice per group; for proliferation assays, $n = 4$ WT;bmWT mice and $n = 5$ WT;bm*Hcrtr1*$^{GFP/GFP}$ mice). **k**, Concentration of CSF1 in the bone marrow of wild-type mice transplanted with wild-type or *Hcrtr1*$^{GFP/GFP}$ bone marrow cells ($n = 4$ WT;bmWT mice; $n = 5$ WT;bm*Hcrtr1*$^{GFP/GFP}$ mice). **l**, Images of cross-sections of aortic roots stained with oil red O and quantification of atherosclerosis in *Ldlr*$^{-/-}$ mice transplanted with wild-type or *Hcrtr1*$^{GFP/GFP}$ bone marrow cells and fed a high-cholesterol diet for 12 weeks ($n = 8$ *Ldlr*$^{-/-}$;bmWT mice ; $n = 9$ *Ldlr*$^{-/-}$;bm*Hcrtr1*$^{GFP/GFP}$ mice). Data are mean ± s.e.m., $^{*}P < 0.05$, $^{**}P < 0.01$, $^{***}P < 0.001$, two-tailed Mann–Whitney *U*-tests unless otherwise indicated. ND, not detected.

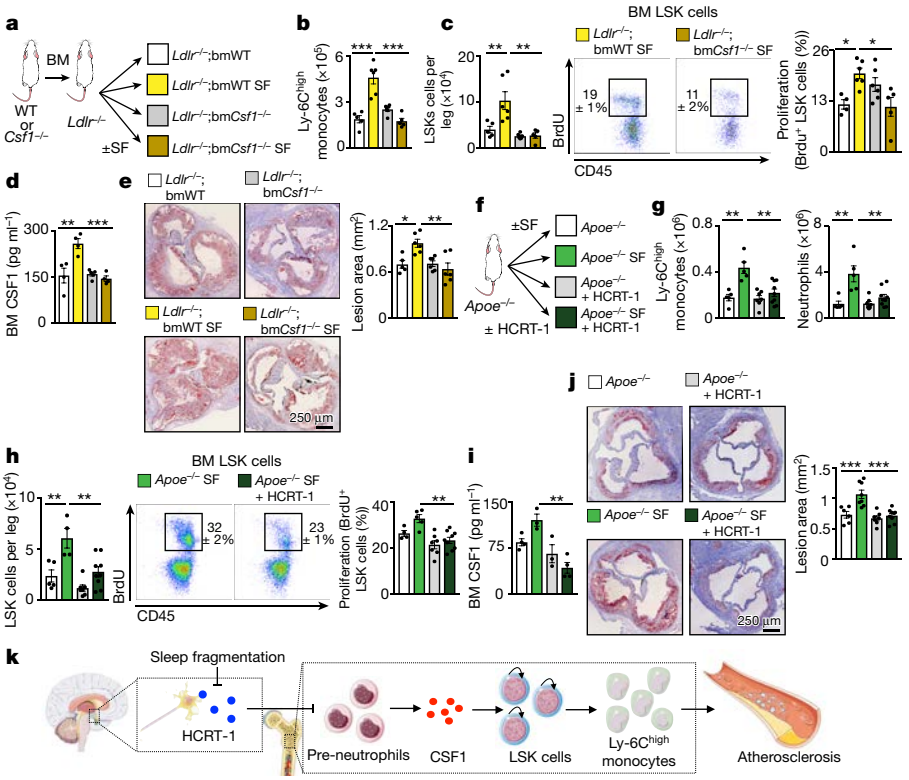

Fig. 4 | Haematopoietic CSF1 deletion or hypocretin supplementation protects against sleep fragmentation-induced haematopoiesis and atherosclerosis. **a**, Schematic of chimeric *Ldlr*$^{-/-}$ mice with wild-type or *Csf1*$^{-/-}$ haematopoietic cells subjected to sleep fragmentation. **b**, Quantification of blood Ly-6C^{high} monocytes in chimeric mice ($n = 5$ *Ldlr*$^{-/-}$;bmWT mice; $n = 6$ *Ldlr*$^{-/-}$;bmWT SF mice; $n = 6$ *Ldlr*$^{-/-}$;bm*Csf1*$^{-/-}$ mice; $n = 5$ *Ldlr*$^{-/-}$;bm*Csf1*$^{-/-}$ SF mice). **c**, Quantification of bone marrow LSK cells and BrdU incorporation in chimeric mice (for LSK cells per leg, $n = 5$ *Ldlr*$^{-/-}$;bmWT mice; $n = 6$ *Ldlr*$^{-/-}$;bmWT SF mice; $n = 6$ *Ldlr*$^{-/-}$;bm*Csf1*$^{-/-}$ mice; $n = 5$ *Ldlr*$^{-/-}$;bm*Csf1*$^{-/-}$ SF mice; for proliferation assays, $n = 4$ *Ldlr*$^{-/-}$;bmWT mice; $n = 6$ *Ldlr*$^{-/-}$;bmWT SF mice; $n = 6$ *Ldlr*$^{-/-}$;bm*Csf1*$^{-/-}$ mice; $n = 5$ *Ldlr*$^{-/-}$;bm*Csf1*$^{-/-}$ SF mice). **d**, Concentration of CSF1 in the bone marrow of chimeric mice ($n = 4$ *Ldlr*$^{-/-}$;bmWT mice; $n = 4$ *Ldlr*$^{-/-}$;bmWT SF mice; $n = 5$ *Ldlr*$^{-/-}$;bm*Csf1*$^{-/-}$ mice; $n = 4$ *Ldlr*$^{-/-}$;bm*Csf1*$^{-/-}$ SF mice). **e**, Images of cross-sections of aortic roots stained with oil red O and assessment of atherosclerosis in chimeric mice after 16 weeks of high-cholesterol diet ($n = 5$ *Ldlr*$^{-/-}$;bmWT mice; $n = 6$ *Ldlr*$^{-/-}$;bmWT SF mice; $n = 6$ *Ldlr*$^{-/-}$;bm*Csf1*$^{-/-}$ mice; $n = 6$ *Ldlr*$^{-/-}$;bm*Csf1*$^{-/-}$ SF mice). **f**, Schematic of mice subjected to 16 weeks of sleep fragmentation that received HCRT-1 or saline through osmotic mini-pumps. **g**, Quantification of blood Ly-6C^{high} monocytes and neutrophils ($n = 5$ *Apoe*$^{-/-}$ mice; $n = 5$ *Apoe*$^{-/-}$ SF mice; $n = 7$ *Apoe*$^{-/-}$ mice treated with HCRT-1; $n = 9$ *Apoe*$^{-/-}$ SF mice treated with HCRT-1). **h**, LSK cells and BrdU incorporation in the bone marrow of SF mice with HCRT-1 supplementation ($n = 5$ *Apoe*$^{-/-}$ mice; $n = 4$ *Apoe*$^{-/-}$ SF mice; $n = 7$ *Apoe*$^{-/-}$ mice treated with HCRT-1; $n = 9$ *Apoe*$^{-/-}$ SF mice treated with HCRT-1). **i**, Bone marrow CSF1 levels ($n = 4$ *Apoe*$^{-/-}$ mice; $n = 3$ *Apoe*$^{-/-}$ SF mice; $n = 3$ *Apoe*$^{-/-}$ mice treated with HCRT-1; $n = 4$ *Apoe*$^{-/-}$ SF mice treated with HCRT-1). **j**, Images of cross-sections of aortic roots stained with oil red O and quantification of atherosclerotic lesion areas ($n = 6$ *Apoe*$^{-/-}$ mice; $n = 8$ *Apoe*$^{-/-}$ SF mice; $n = 7$ *Apoe*$^{-/-}$ mice treated with HCRT-1; $n = 9$ *Apoe*$^{-/-}$ SF mice treated with HCRT-1). **k**, Model of the role of sleep in regulating hypocretin production, haematopoiesis and atherosclerosis. The illustration was modified from Servier Medical Art (http://smart.servier.com/), licensed under a Creative Common Attribution 3.0 Generic License. Data are mean ± s.e.m., $^{*}P < 0.05$, $^{**}P < 0.01$, $^{***}P < 0.001$, one-way ANOVA.

pre-neutrophils as GFP^{+} and thus able to express the receptor (Fig. 3c and Extended Data Fig. 9b).

The observation that bone marrow CXCR4^{+}CXCR2^{-} pre-neutrophils expressed *Hcrtr1* was notable, because these cells reside in close proximity to haematopoietic progenitors[28]. Moreover, neutrophils produce substantial amounts of colony stimulating factor-1 (CSF1), which promotes bone marrow myeloid-biased haematopoiesis[30] (Fig. 3d). In part because pre-neutrophils sorted from wild-type mice expressed less *Csf1* compared to mature neutrophils (Fig. 3e), we tested whether hypocretin can control haematopoiesis through HCRTR1^{+} pre-neutrophil-derived CSF1. In vitro, hypocretin limited the capacity of pre-neutrophils to produce CSF1 in response to lipopolysaccharides (Fig. 3f and Extended Data Fig. 9c). Ex vivo, pre-neutrophils and neutrophils sorted from *Hcrt*$^{-/-}$ mice contained more *Csf1* mRNA and secreted more CSF1 protein than cells sorted from wild-type mice (Fig. 3g and Extended Data Fig. 9d). In vivo, we found increased levels of CSF1 in the bone marrow of *Hcrt*$^{-/-}$ mice and *Apoe*$^{-/-}$ mice subjected to sleep fragmentation (Fig. 3h). Indeed, sleep fragmentation increased bone marrow CSF1 production without substantially changing the expression of other growth factors (Extended Data Fig. 9e).

Because bone marrow non-haematopoietic cells do not express HCRTR1 (Fig. 3a) but produce CSF1 (Fig. 3d), we asked whether hypocretin-mediated control of leukocyte-derived CSF1 is important. First, we lethally irradiated wild-type mice and transplanted them with bone marrow cells from either wild-type or *Hcrtr1*-knockout reporter (*Hcrtr1*$^{GFP/GFP}$) mice. Chimaeras with *Hcrtr1*$^{GFP/GFP}$ bone marrow developed monocytosis (Fig. 3i), along with an increased number of LSK cells, increased proliferation of LSK cells (Fig. 3j) and increased levels of CSF1 in the bone marrow (Fig. 3k). Second, we transplanted *Ldlr*$^{-/-}$ mice with *Hcrtr1*$^{GFP/GFP}$ bone marrow and noted augmented atherosclerosis (Fig. 3l). Third, we lethally irradiated wild-type or *Hcrt*$^{-/-}$ mice and transplanted them with bone marrow cells from either wild-type or *Csf1*$^{-/-}$ mice (Extended Data Fig. 10a). As expected, wild-type mice had relatively few Ly-6C^{high} monocytes regardless of bone marrow source. However, whereas *Hcrt*$^{-/-}$ mice reconstituted with wild-type bone marrow cells developed leukocytosis, *Hcrt*$^{-/-}$ mice reconstituted with *Csf1*$^{-/-}$ bone marrow cells had relatively few Ly-6C^{high} monocytes, limited haematopoietic progenitors and proliferation, and reduced concentrations of CSF1 (Extended Data Fig. 10b–f). Notably, neutrophil numbers remained high in

Hcrt$^{-/-}$ mice reconstituted with *Csf1*$^{-/-}$ bone marrow, which indicates that neutrophilia in *Hcrt*$^{-/-}$ mice was not directly related to the interactions between HCRT and leukocyte control of CSF1, an observation we confirmed in wild-type (WT) mice reconstituted with bone marrow (bm) from *Hcrtr1*$^{GFP/GFP}$ mice (hereafter WT;bm*Hcrtr1*$^{GFP/GFP}$ mice) (Extended Data Fig. 9f). Fourth, we induced atherogenesis in wild-type and *Hcrt*$^{-/-}$ chimaeras reconstituted with either wild-type or *Csf1*$^{-/-}$ bone marrow by overexpressing PCSK9 and feeding the mice a high-cholesterol diet. We found that *Hcrt*$^{-/-}$;bmWT mice developed larger lesions than *Hcrt*$^{-/-}$;bm*Csf1*$^{-/-}$ mice (Extended Data Fig. 10g–i). These data agree with the hypothesis that hypocretin controls monocytosis and atherosclerosis by mediating CSF1 production by pre-neutrophils.

Finally, we sought to explore the role of hypocretin in atherosclerosis and sleep fragmentation. We generated *Ldlr*$^{-/-}$ mice with either wild-type or *Csf1*$^{-/-}$ bone marrow, and subjected the chimaeras to sleep fragmentation (Fig. 4a). *Ldlr*$^{-/-}$ mice with wild-type bone marrow that were subjected to sleep fragmentation developed monocytosis through increased haematopoiesis, increased proliferation of LSK cells and increased levels of CSF1 in the bone marrow—processes that together led to bigger atherosclerotic lesions—whereas the absence of bone marrow-derived CSF1 reduced these parameters in SF mice (Fig. 4b–e). Moreover, we delivered hypocretin to the periphery of *Apoe*$^{-/-}$ mice subjected to sleep fragmentation (Fig. 4f). Compared to controls, *Apoe*$^{-/-}$ mice subjected to sleep fragmentation that received hypocretin had fewer monocytes and neutrophils in the blood (Fig. 4g), reduced proliferation and a reduction in the number of LSK cells in the bone marrow (Fig. 4h), lower levels of CSF1 in the bone marrow (Fig. 4i) and smaller lesions (Fig. 4j). These results demonstrate that hypocretin loss during sleep fragmentation aggravates haematopoiesis and atherosclerosis.

Our data indicate that sleep protects against atherosclerosis. Undisturbed sleep maintains proper hypothalamic release of hypocretin, which limits pre-neutrophil CSF1 in the bone marrow, thereby curtailing haematopoiesis and atherosclerosis. This neuro-immune axis directly connects sleep to immune function and cardiovascular disease (Fig. 4k).

Online content

Any methods, additional references, Nature Research reporting summaries, source data, statements of data availability and associated accession codes are available at https://doi.org/10.1038/s41586-019-0948-2.

Received: 18 February 2018; Accepted: 7 January 2019;
Published online: 13 February 2019

1. Hublin, C., Partinen, M., Koskenvuo, M. & Kaprio, J. Sleep and mortality: a population-based 22-year follow-up study. *Sleep* **30**, 1245–1253 (2007).
2. Cappuccio, F. P., Cooper, D., D'Elia, L., Strazzullo, P. & Miller, M. A. Sleep duration predicts cardiovascular outcomes: a systematic review and meta-analysis of prospective studies. *Eur. Heart J.* **32**, 1484–1492 (2011).
3. Hafner, M., Stepanek, M., Taylor, J., Troxel, W. M. & van Stolk, C. Why sleep matters—the economic costs of insufficient sleep: a cross-country comparative analysis. *Rand Health Q.* **6**, 11 (2017).
4. Ford, E. S., Cunningham, T. J. & Croft, J. B. Trends in self-reported sleep duration among US adults from 1985 to 2012. *Sleep* **38**, 829–832 (2015).
5. Cappuccio, F. P. et al. Meta-analysis of short sleep duration and obesity in children and adults. *Sleep* **31**, 619–626 (2008).
6. Shan, Z. et al. Sleep duration and risk of type 2 diabetes: a meta-analysis of prospective studies. *Diabetes Care* **38**, 529–537 (2015).
7. Blask, D. E. Melatonin, sleep disturbance and cancer risk. *Sleep Med. Rev.* **13**, 257–264 (2009).
8. Carreras, A. et al. Chronic sleep fragmentation induces endothelial dysfunction and structural vascular changes in mice. *Sleep* **37**, 1817–1824 (2014).
9. Swirski, F. K. & Nahrendorf, M. Leukocyte behavior in atherosclerosis, myocardial infarction, and heart failure. *Science* **339**, 161–166 (2013).
10. Scheiermann, C. et al. Adrenergic nerves govern circadian leukocyte recruitment to tissues. *Immunity* **37**, 290–301 (2012).
11. He, W. et al. Circadian expression of migratory factors establishes lineage-specific signatures that guide the homing of leukocyte subsets to tissues. *Immunity* **49**, 1175–1190 (2018).
12. Lasselin, J., Rehman, J. U., Åkerstedt, T., Lekander, M. & Axelsson, J. Effect of long-term sleep restriction and subsequent recovery sleep on the diurnal rhythms of white blood cell subpopulations. *Brain Behav. Immun.* **47**, 93–99 (2015).
13. Geovanini, G. R. et al.; Association between obstructive sleep apnea and cardiovascular risk factors: variation by age, sex, and race. The multi-ethnic study of atherosclerosis. *Ann. Am. Thorac. Soc.* **15**, 970–977 (2018).
14. Heidt, T. et al. Chronic variable stress activates hematopoietic stem cells. *Nat. Med.* **20**, 754–758 (2014).
15. Li, X., Marchant, N. J. & Shaham, Y. Opposing roles of cotransmission of dynorphin and hypocretin on reward and motivation. *Proc. Natl Acad. Sci. USA* **111**, 5765–5766 (2014).
16. Fu, L. Y., Acuna-Goycolea, C. & van den Pol, A. N. Neuropeptide Y inhibits hypocretin/orexin neurons by multiple presynaptic and postsynaptic mechanisms: tonic depression of the hypothalamic arousal system. *J. Neurosci.* **24**, 8741–8751 (2004).
17. Scammell, T. E., Arrigoni, E. & Lipton, J. O. Neural circuitry of wakefulness and sleep. *Neuron* **93**, 747–765 (2017).
18. Latorre, D. et al. T cells in patients with narcolepsy target self-antigens of hypocretin neurons. *Nature* **562**, 63–68 (2018).
19. Hartmann, F. J. et al. High-dimensional single-cell analysis reveals the immune signature of narcolepsy. *J. Exp. Med.* **213**, 2621–2633 (2016).
20. Ibrahim, N. E. et al. circulating concentrations of orexin A predict left ventricular myocardial remodeling. *J. Am. Coll. Cardiol.* **68**, 2238–2240 (2016).
21. Perez, M. V. et al. Systems genomics identifies a key role for hypocretin/orexin receptor-2 in human heart failure. *J. Am. Coll. Cardiol.* **66**, 2522–2533 (2015).
22. Adam, J. A. et al. Decreased plasma orexin-A levels in obese individuals. *Int. J. Obes. Relat. Metab. Disord.* **26**, 274–276 (2002).
23. Ohayon, M. M. Narcolepsy is complicated by high medical and psychiatric comorbidities: a comparison with the general population. *Sleep Med.* **14**, 488–492 (2013).
24. Mochizuki, T. et al. Behavioral state instability in orexin knock-out mice. *J. Neurosci.* **24**, 6291–6300 (2004).
25. Sellayah, D., Bharaj, P. & Sikder, D. Orexin is required for brown adipose tissue development, differentiation, and function. *Cell Metab.* **14**, 478–490 (2011).
26. Aspelund, A. et al. A dural lymphatic vascular system that drains brain interstitial fluid and macromolecules. *J. Exp. Med.* **212**, 991–999 (2015).
27. Louveau, A. et al. Structural and functional features of central nervous system lymphatic vessels. *Nature* **523**, 337–341 (2015).
28. Evrard, M. et al. Developmental analysis of bone marrow neutrophils reveals populations specialized in expansion, trafficking, and effector functions. *Immunity* **48**, 364–379 (2018).
29. Li, S., Franken, P. & Vassalli, A. Bidirectional and context-dependent changes in theta and gamma oscillatory brain activity in noradrenergic cell-specific hypocretin/orexin receptor 1-KO mice. *Sci. Rep.* **8**, 15474 (2018).
30. Mossadegh-Keller, N. et al. M-CSF instructs myeloid lineage fate in single haematopoietic stem cells. *Nature* **497**, 239–243 (2013).

Acknowledgements This work was supported in part by NIH grants R35 HL135752, R01 HL128264, P01 HL131478, an American Heart Association Established Investigator Award, and the Patricia and Scott Eston MGH Research Scholar (to F.K.S.); NIH grant R35 HL139598 (to M.N.); Swiss National Science Foundation grants 31003A_125323 and 31003A_144282 (to A.V.); a CIHR postdoctoral fellowship and a Banting postdoctoral fellowship (to C.S.M.); the doctoral program Cell Communication in Health and Disease (CCHD) funded by the Austrian Science Fund (to M.G.K.); a Swedish Research Council postdoctoral fellowship (to S.R.); an American Heart Association postdoctoral fellowship (to S.H.); a postdoctoral fellowship from the Fondation pour la Recherche Medicale (to C.V.); the German Research Foundation (DFG; 331536185 to F.K. and 398190272 to W.C.P.); and a Boehringer-Ingelheim-Fonds MD fellowship (to L.H.). We thank A. Lichtman for providing the PCSK9 adenovirus, D. Scadden for providing stromal cell reporter mice and K. Joyes for editing the manuscript.

Reviewer information *Nature* thanks P. S. Frenette, V. Papayannopoulos, A. R. Tall and A. Yamanaka for their contribution to the peer review of this work.

Author contributions C.S.M. conceived the project, designed and performed experiments, analysed and interpreted data, made the figures and wrote the manuscript; M.G.K. designed and performed experiments, and analysed and interpreted data; S.R., S.H., A.V., A.A., C.V., C.T.C., J.E.M., F.K., W.C.P., V.F., A.M.F., A.F.G., L.H., Y.I. and F.F.H. performed experiments; A.V., C.J.B., P.L., M.T., T.E.S. and M.N. provided intellectual input and edited the manuscript; A.V., M.T. and T.E.S. provided materials; F.K.S. conceived the project, designed experiments, interpreted data and wrote the manuscript.

Competing interests The authors declare no competing interests.

Additional information
Extended data is available for this paper at https://doi.org/10.1038/s41586-019-0948-2.
Supplementary information is available for this paper at https://doi.org/10.1038/s41586-019-0948-2.
Reprints and permissions information is available at http://www.nature.com/reprints.
Correspondence and requests for materials should be addressed to F.K.S.
Publisher's note: Springer Nature remains neutral with regard to jurisdictional claims in published maps and institutional affiliations.

METHODS

Animals. Wild-type C57BL/6J, Apoe^{tm1Unc} (*Apoe*$^{-/-}$), Ldlr^{tm1Her}/J (*Ldlr*$^{-/-}$) and Csf1^{op} (*Csf1*$^{-/-}$) mice were purchased from The Jackson Laboratory. *Hcrt*$^{-/-}$ mice[31] were provided by T. Scammell (Department of Neurology, Beth Israel Deaconess Medical Center) and bred in-house. *Hcrtr1*$^{GFP/GFP}$ mice[29,32] were provided by A. Vassalli (Department of Physiology, University of Lausanne). Stromal cell *Nestin-GFP* mice[33,34], *Lepr-cre-Rosa26-eYFP* mice[35,36] and OCN-GFP^{topaz} reporter mice[37] were provided by D. Scadden (Department of Stem Cell and Regenerative Biology, Harvard University and the Center for Regenerative Medicine, Massachusetts General Hospital). Genotyping for each strain was performed as described on the Jackson Laboratory website. Age- and sex-matched animals were used starting at 8–12 weeks of age. For experiments involving *Apoe*$^{-/-}$ and *Ldlr*$^{-/-}$ mice, female mice were used. For all other experiments, both male and female mice were used. All mice were group-housed on a 12:12-h light:dark cycle at 22 °C with free access to food and water. Where appropriate, animals were randomly assigned to interventions. Experiments were performed in a blinded fashion. All protocols were approved by the Animal Review Committee at Massachusetts General Hospital (protocol no. 2011N000035 and 2015N000044) and were in compliance with relevant ethical regulations.

In vivo interventions. *Diet. Apoe*$^{-/-}$ mice were fed a high-fat diet (HFD, Harlan Teklad, TD.88137) and *Ldlr*$^{-/-}$ mice were fed a high-cholesterol diet (HCD, Research Diets, D12331). Mice were injected by intravenous injection with 5×10^{11}U of adv-PCSK9 virus after which the mice were fed the HCD immediately after virus injection. Unless otherwise indicated, mice were fed a regular chow diet.

Sleep fragmentation. For sleep fragmentation studies, mice were placed in a sleep fragmentation chamber (Lafayette Instrument) at the same time as initiation of special diet feeding. The sweep bar moved along the bottom of the cage every 2 min during the light cycle (ZT0–12). The sweep bar automatically shut off and was stationary during the dark cycle (ZT12–24). Control mice that received undisturbed sleep were placed in sleep fragmentation chambers with stationary sweep bars. For the control experiment in Extended Data Fig. 1f–h, the sweep bar moved along the bottom of the cage every 2 min during the dark cycle (ZT12–0) and automatically shut off and was stationary during the light cycle (ZT0–12).

Interventions. For studies on microbiota, mice were treated with an antibiotic cocktail (0.1% ampicillin, 0.1% metronidazole, 0.05% vancomycin and 0.1% neomycin) in drinking water for 4 weeks. Antibiotics-containing drinking water was changed weekly. For hypocretin-supplementation studies, HFD-fed *Apoe*$^{-/-}$ control and sleep fragmentation mice were implanted subcutaneously with osmotic mini-pumps (Alzet) 8 weeks after experiment initiation. Mice were supplemented with hypocretin-1 or saline during weeks 8 to 16 of the experiment. Mice were randomly assigned a pump containing either saline or hypocretin-1 (Sigma Aldrich) delivered at 50 nmol h^{-1} kg^{-1}. Pumps were replaced after four weeks.

Parabiosis. The procedure was conducted as previously described[38–40]. In brief, age-, sex- and weight-matched animals were used and housed together for at least 14 days before surgery. The corresponding lateral aspects of each mouse were shaved, incisions were made from the forelimb joint to the hindlimb joint and the subcutaneous fascia was bluntly dissected to create 0.5 cm of free skin. Fore- and hindlimb joints were joined and the dorsal and ventral skins were approximated by continuous suture using mononylon 5.0 (Ethicon).

Bone marrow transplantation. Mice were lethally irradiated (950 cGy) and reconstituted with 6×10^6 bone marrow cells injected intravenously to generate chimaera groups. Mice were allowed to recover for eight weeks before further manipulation.

Intra-cisterna magna injection. The procedure was conducted as previously described[41]. Mice were anaesthetized and the skin of the neck was shaved and disinfected with 70% ethanol. Mice were placed in a stereotactic frame (Stoelting) to secure their heads. A skin incision was made at the back of the neck and muscle layers were retracted to expose the cisterna magna. Using a Hamilton syringe, 2 μg of hypocretin-1 dissolved in 5 μl of PBS was injected into the CSF-filled cisterna magna compartment. After injection the needle was left in place for 5 min before removal to prevent backflow. The skin of the neck was sutured closed and mice were allowed to recover.

Cells. *Cell collection.* Peripheral blood was collected by retro-orbital bleeding and red blood cells were lysed in RBC lysis buffer (Biolegend). Aortas, lungs, livers and hearts were excised after PBS (Thermo Fisher Scientific) perfusion, minced and digested with 450 U ml^{-1} collagenase I, 125 U ml^{-1} collagenase XI, 60 U ml^{-1} DNase I and 60 U ml^{-1} hyaluronidase (Sigma-Aldrich) in PBS for 20 min (liver), 40 min (aorta) or 1 h (heart and lung) at 37 °C. Spleens were crushed through a 40-μm cell strainer and red blood cells were lysed with RBC lysis buffer. Bone marrow cells were collected by flushing bones with PBS, after which a single-cell suspension was created by passing cells through a 26-gauge needle and red blood cells were lysed with RBC lysis buffer. Total viable cell numbers were counted using trypan blue (Cellgro, Mediatech) or counting beads (Thermo Fisher Scientific).

Cell sorting. Bone marrow cell suspensions were stained to identify the indicated cell populations and cells were sorted on a FACS Aria II cell sorter (BD Biosciences) directly into collection medium.

Flow cytometry. Single-cell suspensions were stained in PBS supplemented with 2% FBS and 0.5% BSA. The following monoclonal antibodies were used for flow cytometry analyses: anti-CD45 (BioLegend, clone30-F11, 103147, lot B243834), anti-CD45.1 (BioLegend, clone A20, 110708), anti-CD45.2 (BioLegend, clone 104, 109802), anti-CD3 (BioLegend, clone 17A2, 100206), anti-CD90.2 (BioLegend, clone 53-2.1, 105308, lot B260050), anti-CD19 (BioLegend, clone 6D5, 115508, lot B226581), anti-B220 (BD Biosciences, clone RA3-6B2, 553089, lot 6012954), anti-NK1.1 (BioLegend, clone PK136, 108708), anti-Ly-6G (BioLegend, clone 1A8, 127614, lot B259670), anti-Ly-6C (BioLegend, AL-21, 128006, lot B247728), anti-MHCII (BioLegend, clone M5/114.152, 107602, lot B217859), anti-F4/80 (Biolegend, clone BM8, 123114, lot B237342), anti-CD11b (BioLegend, clone M1/70, 101226, lot B238268), anti-CD115 (BioLegend, clone AFS98, 135517, lot B265220), anti-Ter119 (BioLegend, clone TER-119, 116208, lot B220899), anti-CD34 (eBioscience, clone RAM34, 11-0341-85, lot E00265-1634), anti-CD49b (BioLegend, clone DX5, 1089008, lot B258302), anti-CD11c (BioLegend, clone N418, 117310, lot B206713), anti-IL-7Rα (BioLegend, clone SB/199, 121112, lot B189668), anti-CD16/32 (BioLegend, clone 93, 101324, lot B250025), anti-CD150 (BioLegend, clone TC15-12F12.2, 115922, lot B220585), anti-Kit (BioLegend, clone 2B8, 105814, lot B252918), anti-CD135 (BioLegend, clone A2F10, 135310, lot B234045), anti-CD48 (BioLegend, clone HM48-1, 103426, lot B236445), anti-Sca1 (BioLegend, clone D7, 108126, lot B234288), anti-CD8 (BD Bioscience, clone 53-6.7, 553035, lot 2296946), anti-CD4 (BioLegend, clone GK1.5, 100428, lot B237336), anti-SiglecF (BD Pharmingen, clone E50-2440, 562680, lot 7054789), anti-CXCR4 (Invitrogen, clone 2B11, 12-9991-81, lot B251481), anti-CXCR2 (BioLegend, clone SA044G4, 149307, lot B251481), anti-BrdU (eBioscience, clone BU20A, 17-5071-42, lot 4319920). All antibodies were used in a 1:700 dilution. Viable cells were identified as unstained with Zombie Aqua (BioLegend). Cells were identified as (1) Ly-6C^{high} monocytes (CD45$^+$Lin1$^-$CD11b$^+$CD115$^+$F4/80$^-$Ly-6C^{high}), (2) neutrophils (CD45$^+$Lin1$^-$CD11b$^+$Ly-6G$^+$F4/80$^-$), (3) macrophages (CD45$^+$Lin1$^-$CD11b$^+$F4/80$^+$Ly-6C^{low}), (4) B cells (CD45$^+$B220$^+$CD19$^+$F4/80$^-$CD11b$^-$), (5) CD4 T cells (CD45$^+$CD3$^+$CD90$^+$CD4$^+$CD11b$^-$F4/80$^-$), (6) CD8 T cells (CD45$^+$CD3$^+$CD90$^+$CD8$^+$CD11b$^-$F4/80$^-$), (7) LSK cells (CD45$^+$Lin2$^-$Kit$^+$Sca1$^+$), (8) multipotent progenitor (MPP)4 (CD45$^+$Lin2$^-$Kit$^+$Sca1$^+$CD135$^+$CD150$^-$), (9) MPP3 (CD45$^+$Lin2$^-$Kit$^+$Sca1$^+$CD135$^+$CD150$^-$CD48$^+$), (10) MPP2 (CD45$^+$Lin2$^-$Kit$^+$Sca1$^+$CD135$^+$CD150$^+$CD48$^+$), (11) short-term haematopoietic stem cells (CD45$^+$Lin2$^-$Kit$^+$Sca1$^+$CD135$^+$CD150$^-$CD48$^-$), (12) long-term haematopoietic stem cells (CD45$^+$Lin2$^-$Kit$^+$Sca1$^+$CD135$^+$CD150$^+$CD48$^-$), (13) common myeloid progenitor (CD45$^+$Lin2$^-$Kit$^+$Sca1$^-$CD34$^+$CD16/32^{mid}), (14) granulocyte–macrophage progenitor (CD45$^+$Lin2$^-$Kit$^+$Sca1$^-$CD34$^+$CD16/32^{high}CD115$^-$), (15) monocyte–dendritic cell progenitor (CD45$^+$Lin2$^-$Kit$^+$Sca1$^-$CD34$^+$CD16/32^{high}CD115$^+$); for neutrophil populations (CD45$^+$CD3$^-$CD90.2$^-$CD19$^-$NK1.1$^-$SiglecF$^-$CD115$^-$Kit^{low}CD11b$^+$Gr-1$^+$) (16) pre-neutrophils were then separated as Kit^{int}CXCR4$^+$CXCR2$^-$, (17) immature neutrophils as Kit$^-$CXCR4$^-$CXCR2$^-$, and (18) mature neutrophils as Kit$^-$CXCR4$^-$CXCR2$^+$Ly-6G$^+$. Lineages were defined as Lin1: CD3, CD90.2, CD19, NK1.1, Ter119 and Lin2: B220, CD19, CD49b, Ter119, CD90.2, CD11b, CD11c, Ly-6G, IL-7Rα. Osteolineage cells (OCN$^+$) cells were identified as CD45$^-$Ter119$^-$CD31$^-$GFP$^+$ from the bone fraction of OCN–GFP mice. Leptin receptor (Lepr$^+$) cells were identified as CD45$^-$Ter119$^-$CD31$^-$YFP$^+$ form the bone marrow fraction of *Lepr-cre-Rosa26-eYFP* mice. Nestin$^+$ cells were identified as CD45$^-$Ter119$^-$CD31$^-$GFP$^+$ form the bone and bone marrow fraction of *Nestin-GFP* mice. Endothelial cells were identified as CD45$^-$Ter119$^-$CD31$^+$ of the bone marrow fraction of *Lepr-cre-Rosa26-eYFP* mice. Data were acquired on a LSRII (BD Biosciences) and analysed with FlowJo (Tree Star).

BrdU incorporation. To assess cell proliferation, 1 mg BrdU was injected intraperitoneally 2 h before euthanasia. A BrdU flow kit (BD Biosciences) was used to stain BrdU$^+$ cells.

RNA and protein assays. *PCR.* Total RNA was isolated using the RNeasy Mini Kit (Qiagen) or the NucleoSpin RNA XS kit (Takara Bio) according to the manufacturer's instructions. RNase-free DNase Set (Qiagen) was used for DNase digestion during RNA purification. RNA quantity and quality were assessed by Nanodrop for RNA isolated from tissues and with the Aglient RNA 6000 Pico kit (Aglient Technologies) on the Aglient 2100 Bioanalyzer for RNA of fluorescence-activated cell sorting (FACS)-purified cells. cDNA was generated from 1 μg of total RNA per sample using the High Capacity cDNA Reverse Transcription Kit (Applied Biosystems). Quantitative real-time TaqMan PCR was performed using the following TaqMan primers (Applied Biosystems): *Actb* (Mm00607939_s1), *Hcrt* (Mm01964030_s1), *Hcrtr1* (Mm01185776_m1), *Hcrtr2* (Mm01179312_m1), *Csf1* (Mm00432686_m1), *Pmch* (Mm01242886_g1), *Tph2* (Mm00557715_m1), *Agrp* (Mm00475829_g1), *Galp* (Mm00626135_m1), *Ghrl* (Mm00612524_m1), *Gad1* (Mm04207432_g1), *Npy* (Mm01410146_m1), *Pomc* (Mm00435874_m1), *Lepr* (Mm00440181_m1), *Clock* (Mm00455950_m1), *Arntl2* (Mm05549497_m1), *Nr1d2* (Mm01310356_g1), *Csf2* (Mm01290062_m1), *Il1b* (Mm00434228_m1), *Ccl2* (Mm00441242_m1), *Il6* (Mm00446190_m1), *Mpo* (Mm01298424_m1), *Pdny*

(Mm00457573_m1), *Cxcl1* (Mm04207460_m1), *IL2* (Mm00434256_m1), *IL5* (Mm00439646_m1), *IL17* (Mm00439618_m1), *IL23* (Mm00518984_m1), *IL10* (Mm01288386_m1), *Tnf* (Mm00443258_m1), *Il34* (Mm01243248_m1), *Cxcl12* (Mm00445553_m1), *IL3* (Mm00439631_m1), *Csf3* (Mm00438334_m1). PCR was run on a 7500 thermal cycler (Applied Biosystems). Gene expression was normalized to *Actb* and quantified with the $2^{\Delta\Delta C_t}$ method.

Enzyme-linked immunosorbent assay. Hypocretin-1 levels were measured using an enzyme-linked immunosorbent assay (ELISA) kit (Fujifilm Wako Chemicals)[42] and CSF1 (M-CSF) levels were measured using an ELISA kit (Boster Biologial Technology) according to the manufacturers' instructions. Bone marrow ELISAs were performed on bone marrow fluid. In brief, a small hole was made at the tips of the long bones and the marrow was spun out of the bones by centrifugation at 10,000 r.p.m. for 10 min. The supernatant fluid was collected.

Western blot. Total protein was extracted from cells in RIPA lysis buffer with protease and phosphatase inhibitor cocktails. Total protein amount was quantified by Bradford assay. Then, 15 μg of protein was subjected to electrophoresis using a NuPAGE Novex Cel System (Life Technologies) and transferred to a nitrocellulose membrane using the iBlot Gel Transfer System (LifeTechnologies) according to the manufacturer's instructions. Anti-hypocretin receptor-1 antibody (ab68718, Abcam) and anti-β-actin antibody (clone 13E5, Cell Signaling) were used.

Cell culture. For cell-culture experiments, cells were cultured in complete medium (RPMI-1640 supplemented with 10% FBS, 2 mM l-glutamine, 100 U ml^{-1} penicillin and streptomycin, 10 mM HEPES, 50 μM 2-mercaptoethanol, 1 mM sodium pyruvate and 1× nonessential amino acids) and kept in a humidified 5% CO_2 incubator at 37 °C. Neutrophils were sorted with a FACS Aria II and 5×10^5 cells were seeded into 48-well plates in 0.5 ml medium. Cells were then pre-incubated with 0.1 μM hypocretin-1 for 3 h followed by co-treatment with 20 ng ml^{-1} LPS for 3 h as indicated. Cells and medium were collected for downstream analysis.

Myeloid colony-forming unit assay. Single-cell suspensions from bone marrows were prepared and 2×10^4 cells were plated in triplicates in complete methylcellulose medium (MethoCult GF M3534) with or without hypocretin-1 according to the manufacturer's instructions. Colony-forming units were counted after 11 days in a 5% CO_2 incubator at 37 °C.

Histology and μCT. *Aortas.* Aortic roots were dissected and embedded in Tissue-Tek OCT compound (Sakura Finetek), frozen in 2-methylbutane (Fisher Scientific) cooled with dry ice and sectioned into 6-μm slices. To compare lesion size among the groups, sections that captured the maximum lesion area were used. To measure lesion volume, sections were collected beginning at the first appearance of the aortic valves and continuing until lesions were no longer visible. Oil-red-O (Sigma Aldrich) staining was performed to visualize lipid content and measure lesion size. Lesion size was measured using Nanozoomer 2.0RS (Hamamatsu). In brief, the lesion area was quantified by measuring the atherosclerotic plaque of the intima from the endothelial layer to the healthy medium.

Brain. Whole brains were fixed in 10% formalin and embedded in paraffin for histological sectioning. Brains were sectioned coronally and 6-μm slices were collected. After deparaffinization and rehydration of the sections, antigen retrieval was performed and endogenous peroxidase activity was blocked by 3% H_2O_2 solution in dH_2O. Immunohistochemistry was done to stain for hypocretin$^+$ cells using an anti-hypocretin antibody (clone D6G9T, Cell Signaling) diluted in SignalStain Antibody Diluent (Cell Signaling) followed by biotinylated goat anti-rabbit IgG antibody (Vector Laboratories). The hypocretin$^+$ cells were visualized using avidin/biotin-based peroxidase system, VECTASTAIN Elite ABC-HRP Kit (Vector Laboratories) and AEC Substrate Chromogen (DAKO/Agilent). The tissues were counterstained with Harris haematoxylin (Sigma-Aldrich) and all images were captured using Nanozoomer 2.0RS (Hamamatsu). Dynorphin$^+$ cells were identified by staining with dynorphin A antibody (ab82509, Abcam) and AF488-conjugated hypocretin antibody (clone D6G9T, Cell Signaling). Dynorphin$^+$ cells were detected using a biotinylated goat anti-rabbit IgG antibody and streptavidin DyLight 594 (Vector Laboratories). The fluorescence images were captured using a motorized fluorescence microscope Olympus BX63 and processed by FIJI/ImageJ software. Apoptotic cells were investigated using the In situ Cell Death Detection Kit, TMR Red (Sigma-Aldrich) and nuclei were counterstained with DAPI (Thermo Fisher Scientific).

Bone. Femurs were collected and fixed in 4% paraformaldehyde overnight and then scanned by μCT at the MGH Center for Skeletal Research Core (NIHP30AR066261). After scanning, femurs were decalcified in 0.375 M EDTA in PBS for 10 days before paraffin-embedding. Sections were cut and stained with anti-tyrosine hydroxylase antibody (Millipore, AB152).

Behaviour phenotyping. *Open field test.* Mice were individually placed in a white box (50 cm × 50 cm) for 5 min with ambient lighting and videos were recorded. The time the mouse spent within 5 cm of the edge of the box was quantified.

Light–dark box test. Mice were placed in a box in which half the box (25 cm × 25 cm) was black and blocked from light, while the other half was white and exposed to ambient lighting. A dividing wall with a small hole separated the two halves of the box but allowed mice to move freely between the two halves. Videos were recorded for 5 min and the time the mice spent in the white box was quantified.

Y-maze. Mice were allowed to explore two arms of the Y-maze for 5 min before being returned to their home cage. Twenty minutes later, mice were returned to the Y-maze and allowed to explore all three arms for 5 min while being recorded. The time spent in the new arm was quantified. Quantification of behavioural phenotypes was done with ImageJ software.

Statistics. Results are shown as mean ± s.e.m. Statistical tests included unpaired, two-tailed non-parametric Mann–Whitney *U*-tests (when Gaussian distribution was not assumed). For multiple comparisons, a non-parametric multiple-comparisons test comparing the mean rank of each group (when Gaussian distribution was not assumed) was used, or one- or two-way ANOVAs followed by Turkey's test were used. To analyse circadian rhythmicity, cosinor analysis was performed with the following equation[43]: $Y = \text{baseline} + \text{amplitude} \times \cos(\text{frequency} \times X + \text{phase-shift})$. *P* values of 0.05 or less were considered to denote significance.

Reporting summary. Further information on research design is available in the Nature Research Reporting Summary linked to this paper.

Data availability

All relevant data are included in the paper and its Supplementary Information. Source Data for Figs. 1–4 are available in the online version of the paper.

31. Chemelli, R. M. et al. Narcolepsy in orexin knockout mice: molecular genetics of sleep regulation. *Cell* **98**, 437–451 (1999).
32. Vassalli, A., Li, S. & Tafti, M. Comment on "Antibodies to influenza nucleoprotein cross-react with human hypocretin receptor 2". *Sci. Transl. Med.* **7**, 314le2 (2015).
33. Mignone, J. L., Kukekov, V., Chiang, A. S., Steindler, D. & Enikolopov, G. Neural stem and progenitor cells in nestin–GFP transgenic mice. *J. Comp. Neurol.* **469**, 311–324 (2004).
34. Méndez-Ferrer, S. et al. Mesenchymal and haematopoietic stem cells form a unique bone marrow niche. *Nature* **466**, 829–834 (2010).
35. DeFalco, J. et al. Virus-assisted mapping of neural inputs to a feeding center in the hypothalamus. *Science* **291**, 2608–2613 (2001).
36. Ding, L., Saunders, T. L., Enikolopov, G. & Morrison, S. J. Endothelial and perivascular cells maintain haematopoietic stem cells. *Nature* **481**, 457–462 (2012).
37. Bilic-Curcic, I. et al. Visualizing levels of osteoblast differentiation by a two-color promoter–GFP strategy: type I collagen–GFPcyan and osteocalcin–GFPtpz. *Genesis* **43**, 87–98 (2005).
38. Swirski, F. K. et al. Identification of splenic reservoir monocytes and their deployment to inflammatory sites. *Science* **325**, 612–616 (2009).
39. Robbins, C. S. et al. Local proliferation dominates lesional macrophage accumulation in atherosclerosis. *Nat. Med.* **19**, 1166–1172 (2013).
40. Anzai, A. et al. The infarcted myocardium solicits GM-CSF for the detrimental oversupply of inflammatory leukocytes. *J. Exp. Med.* **214**, 3293–3310 (2017).
41. Da Mesquita, S. et al. Functional aspects of meningeal lymphatics in ageing and Alzheimer's disease. *Nature* **560**, 185–191 (2018).
42. Ono, T., Kanbayashi, T., Yoshizawa, K., Nishino, S. & Shimizu, T. Measurement of cerebrospinal fluid orexin-A (hypocretin-1) by enzyme-linked immunosorbent assay: a comparison with radioimmunoassay. *Psychiatry Clin. Neurosci.* **72**, 849–850 (2018).
43. Refinetti, R., Lissen, G. C. & Halberg, F. Procedures for numerical analysis of circadian rhythms. *Biol. Rhythm Res.* **38**, 275–325 (2007).

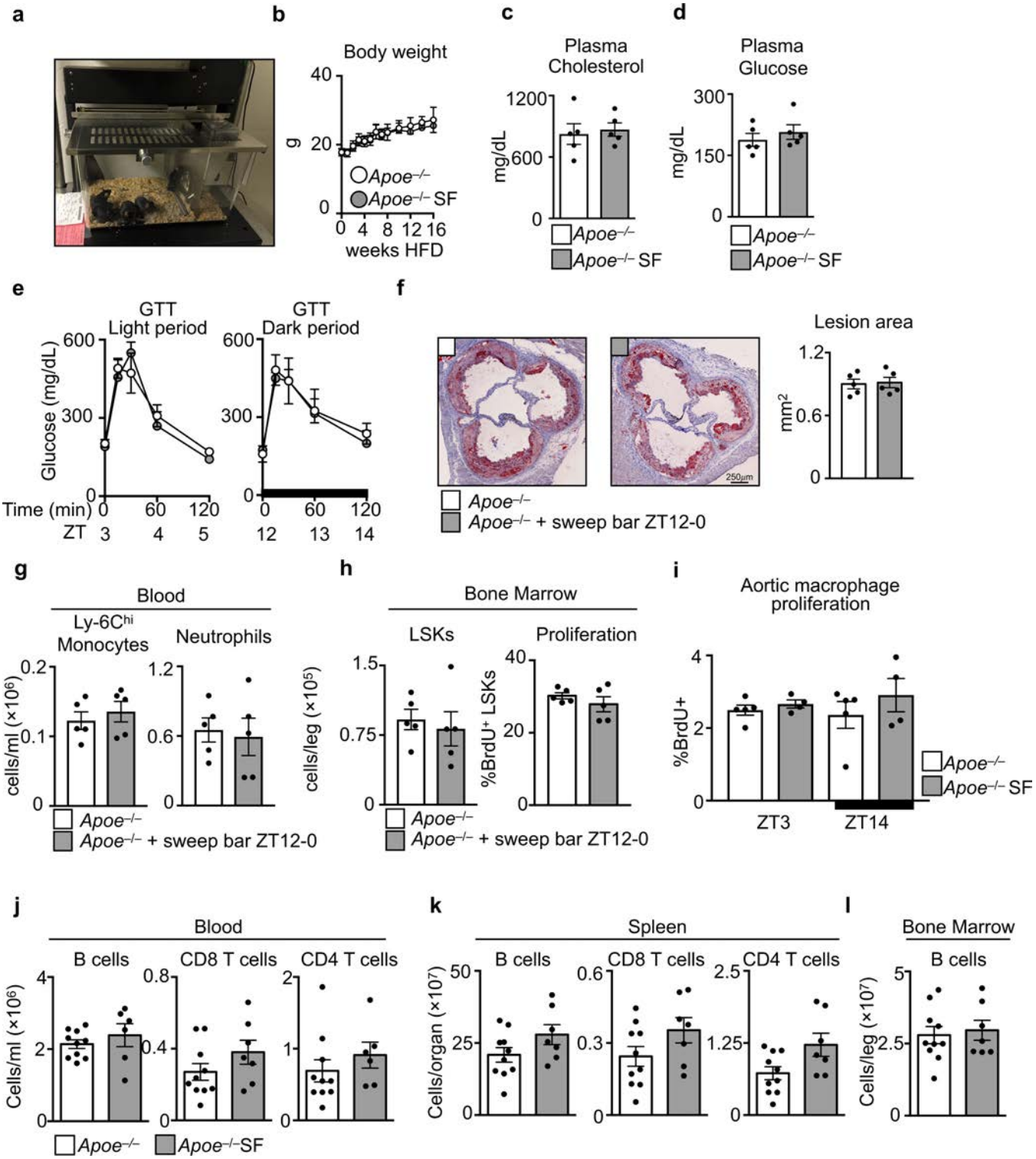

Extended Data Fig. 1 | Effects of sleep fragmentation on metabolic and cellular parameters. a, Image of a sleep fragmentation cage. **b**, Body weight ($n = 10$ per group). **c**, Plasma cholesterol at ZT3 ($n = 5$ per group). **d**, Plasma glucose at ZT3 ($n = 5$ per group). **e**, Glucose tolerance test (GTT) beginning at ZT3 (light period) and ZT12 (dark period) ($n = 4$ per group). **f–h**, *Apoe*$^{-/-}$ mice were placed in sleep fragmentation chambers where the sweep bar operated during the dark period (ZT12–0) when mice are normally awake. Control mice were maintained in sleep fragmentation chambers with a stationary sweep bar. **f**, Assessment of atherosclerosis and lesion area ($n = 5$ per group). **g**, Assessment of blood Ly-6C^{high} monocytes and neutrophils ($n = 5$ per group). **h**, Assessment of bone marrow LSK cells and proliferation ($n = 5$ per group). **i**, Aortic macrophage proliferation in *Apoe*$^{-/-}$ and *Apoe*$^{-/-}$ SF mice after 16 weeks of sleep fragmentation at ZT3 and ZT14 ($n = 5$ *Apoe*$^{-/-}$ mice; $n = 4$ *Apoe*$^{-/-}$ SF mice). **j**, Quantification of B cells, CD4$^+$ T cells and CD8$^+$ T cells in the blood of *Apoe*$^{-/-}$ and *Apoe*$^{-/-}$ SF mice at ZT3 ($n = 10$ *Apoe*$^{-/-}$ mice; for B and CD4 T cells, $n = 6$ *Apoe*$^{-/-}$ SF mice and for CD8 T cells, $n = 7$ *Apoe*$^{-/-}$ SF mice). **k**, Quantification of B cells, CD4$^+$ T cells and CD8$^+$ T cells in the spleen of *Apoe*$^{-/-}$ and *Apoe*$^{-/-}$ SF mice at ZT3 ($n = 10$ *Apoe*$^{-/-}$ mice; $n = 7$ *Apoe*$^{-/-}$ SF mice). **l**, Quantification of B cells in the bone marrow of *Apoe*$^{-/-}$ and *Apoe*$^{-/-}$ SF mice at ZT3 ($n = 10$ *Apoe*$^{-/-}$ mice; $n = 7$ *Apoe*$^{-/-}$ SF mice). Data are mean ± s.e.m.

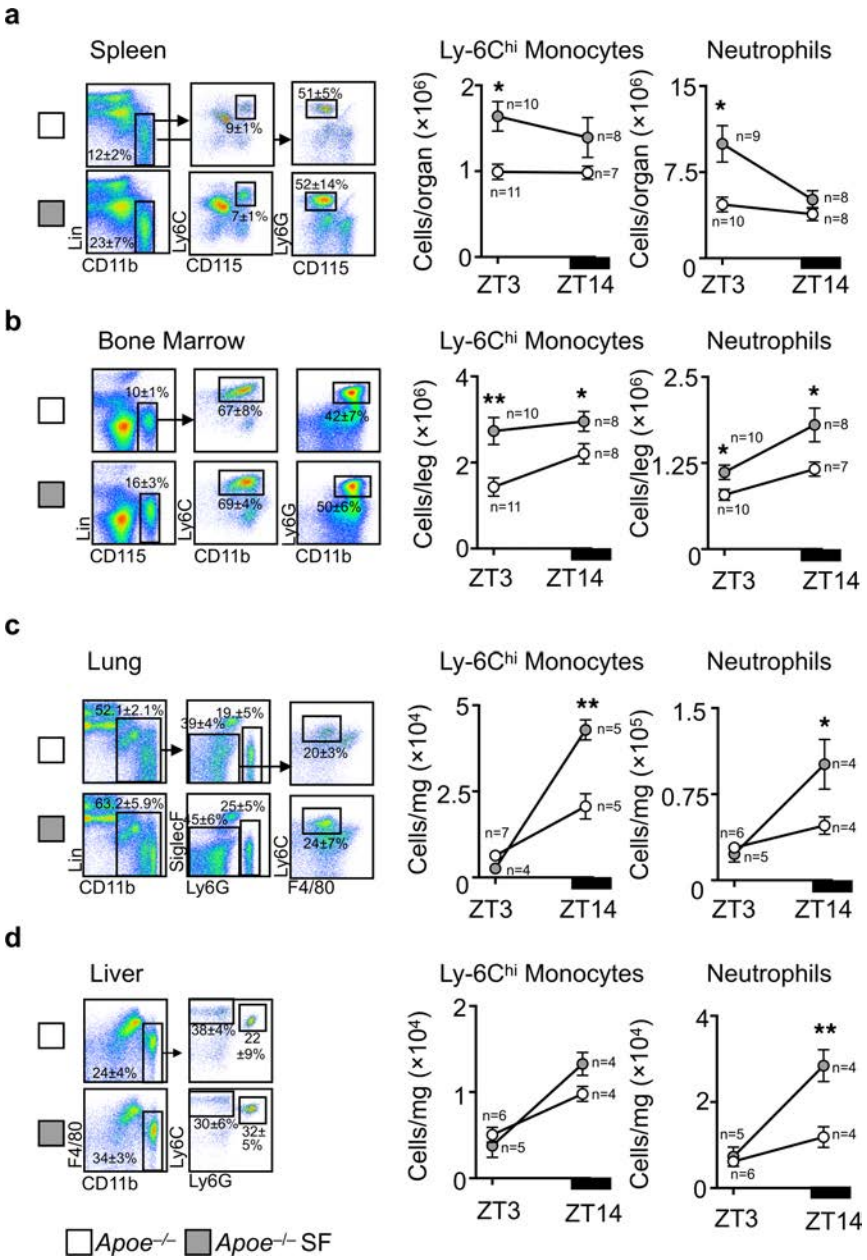

Extended Data Fig. 2 | Sleep and circadian migration of leukocytes. **a**–**d**, Quantification of Ly-6C^{high} monocytes and neutrophils at ZT3 and ZT14 in the spleen (**a**), bone marrow (**b**), lung (**c**) and liver (**d**) of *Apoe*$^{-/-}$ mice and *Apoe*$^{-/-}$ mice after 16 weeks of sleep fragmentation. Group sizes are indicated in the figure. Data are mean ± s.e.m., $*P < 0.05$, $**P < 0.01$, two-way ANOVA.

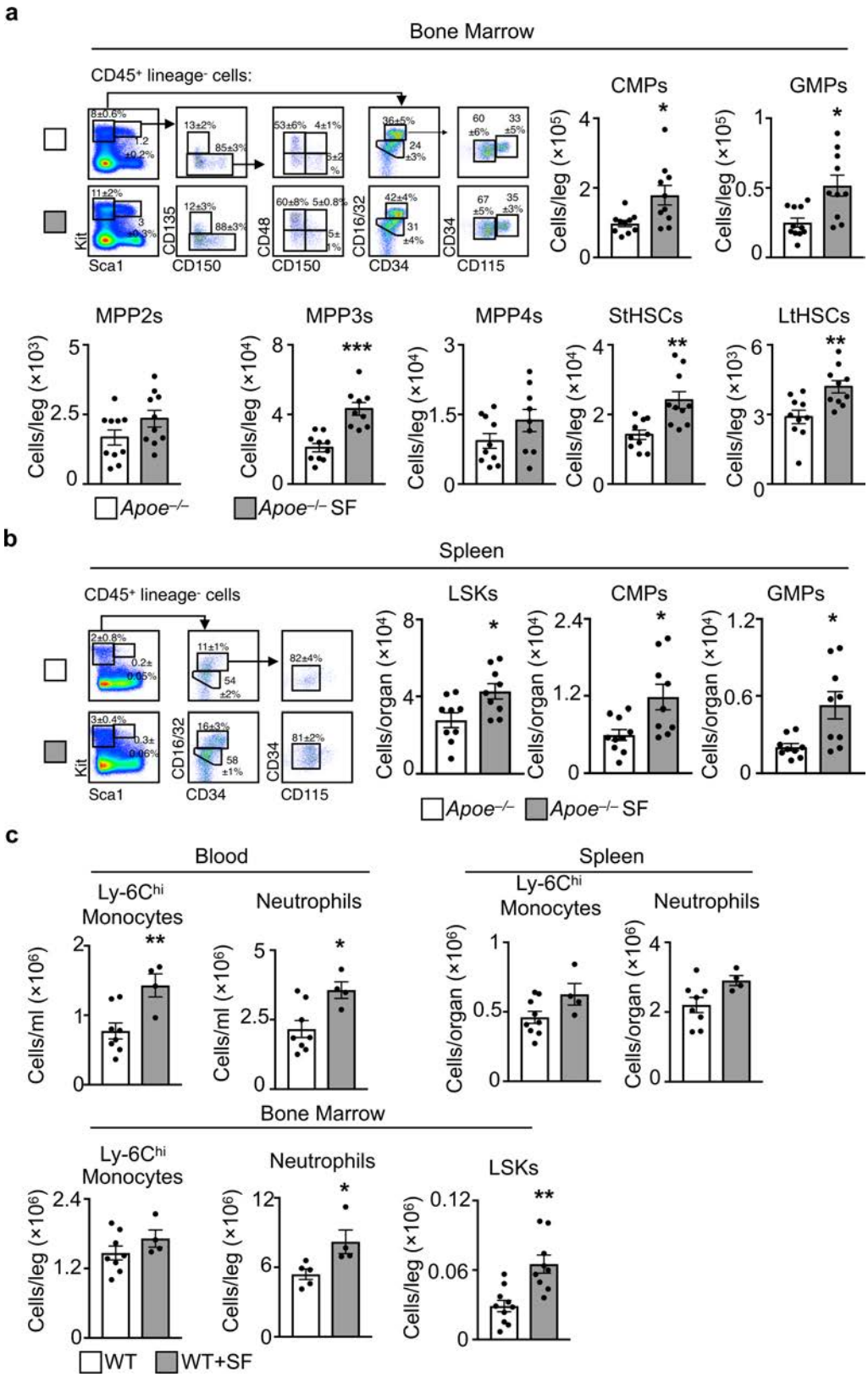

Extended Data Fig. 3 | Sleep-mediated haematopoiesis and extramedullary haematopoiesis. a, Gating strategy and quantification of haematopoietic progenitor cells at ZT3 in the bone marrow ($n = 10$ *Apoe*$^{-/-}$ mice, except for GMPs, $n = 11$ mice; $n = 10$ *Apoe*$^{-/-}$ SF mice, except MPP3 and MPP4, $n = 9$ mice). LtHSCs, long-term haematopoietic stem cells; StHSC, short-term haematopoietic stem cells. **b**, Gating strategy and quantification of haematopoietic progenitor cells at ZT3 in the spleen ($n = 9$ *Apoe*$^{-/-}$ mice, except CMPs, $n = 10$ mice; $n = 9$ *Apoe*$^{-/-}$ SF mice). **c**, C57BL/6 wild-type mice that were fed a regular chow diet were subjected to sleep fragmentation for 16 weeks after which Ly-6C^{high} monocytes, neutrophils and LSK cells were quantified at ZT3 ($n = 8$ wild-type mice, except $n = 9$ mice for spleen Ly-6C^{high} monocytes, $n = 5$ mice for bone marrow neutrophils, $n = 10$ mice for bone marrow LSK cells; $n = 4$ wild-type SF mice, except $n = 9$ mice for bone marrow LSK cells). Data are mean ± s.e.m., $^*P < 0.05$, $^{**}P < 0.01$, $^{***}P < 0.001$, two-tailed Mann–Whitney *U*-tests.

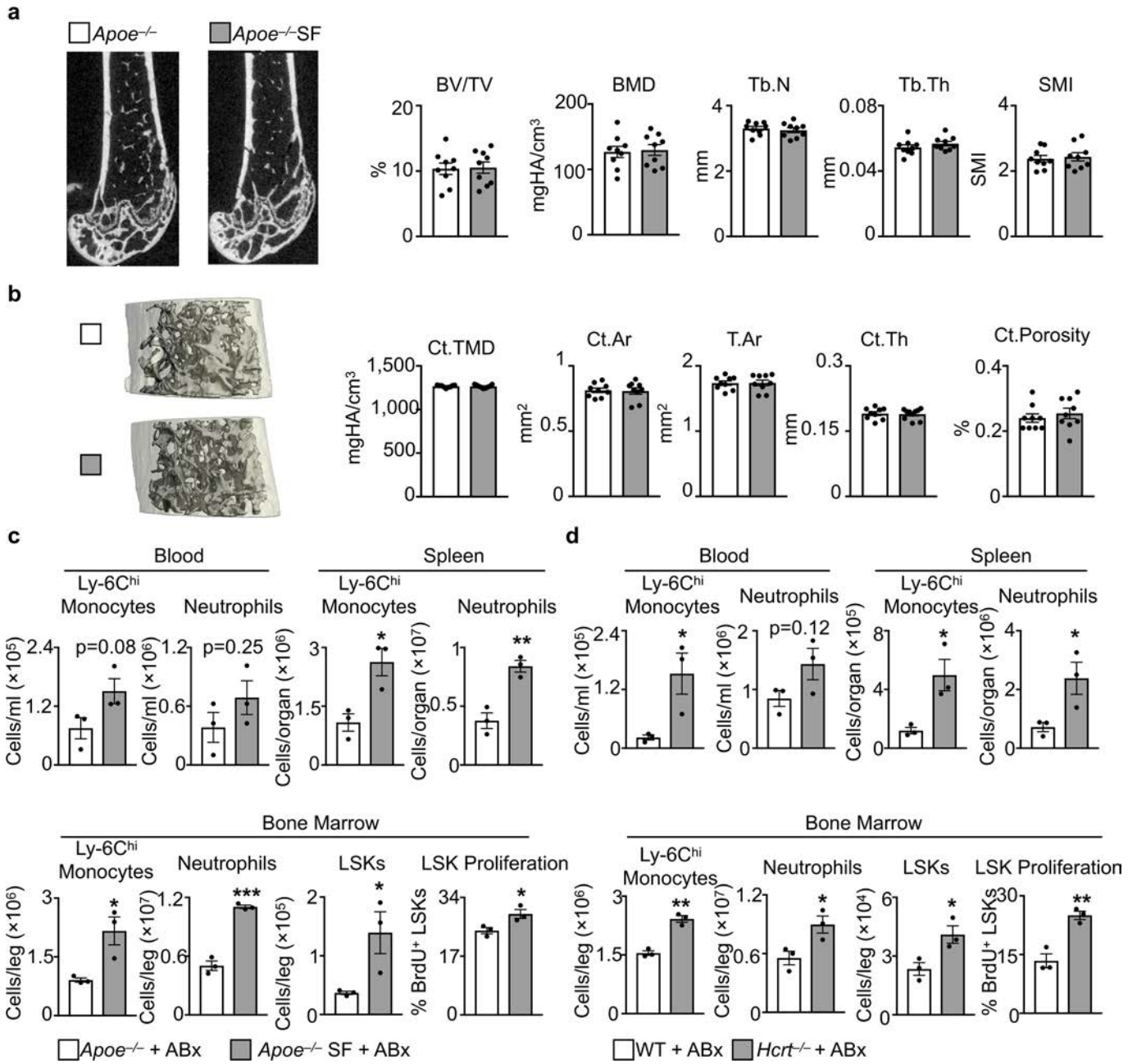

Extended Data Fig. 4 | Sleep fragmentation does not alter bone structure and does not depend on the microbiome. a, **b**, μCT analysis of trabeculae (**a**) and cortical bone structure (**b**) of *Apoe*$^{-/-}$ mice and *Apoe*$^{-/-}$ mice after 16 weeks of sleep fragmentation. The bone volume fraction (BV/TV), bone mineral density (BMD), trabecular number (Tb.N), trabecular thickness (Tb.Th), structural model index (SMI), cortical tissue mineral density (Ct.TMD), cortical area (Ct.Ar), total area (T.Ar), cortical thickness (Ct.Th) and cortical porosity (Ct.Porosity) were analysed ($n = 9$ per group). **c**, **d**, Analysis of leukocytosis in SF (**c**) and *Hcrt*$^{-/-}$ (**d**) mice at ZT3 after receiving a cocktail of antibiotics in drinking water for 4 weeks ($n = 3$ per group). Data are mean ± s.e.m., $^{*}P < 0.05$, $^{**}P < 0.01$, $^{***}P < 0.001$, two-tailed Mann–Whitney *U*-tests.

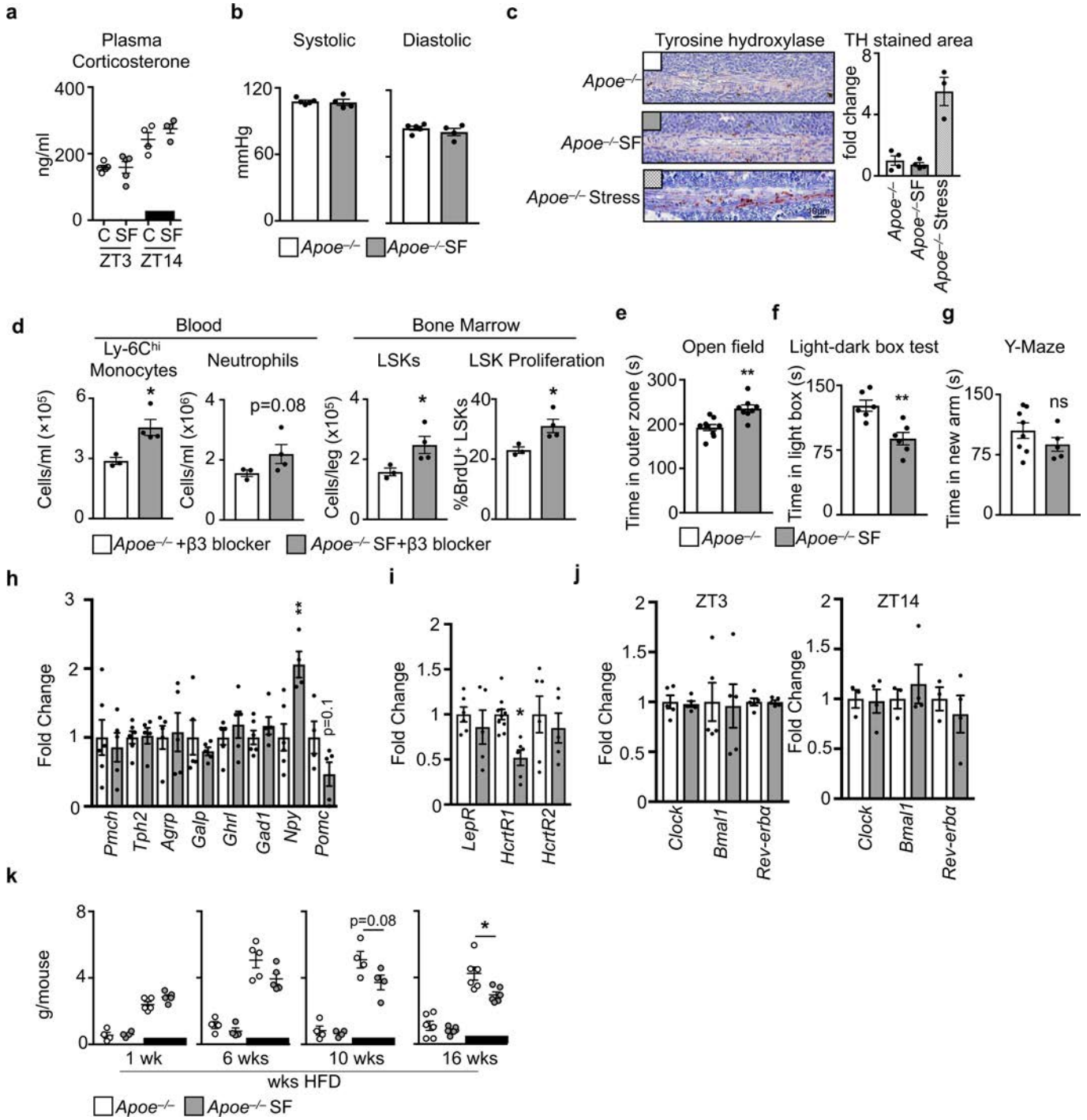

Extended Data Fig. 5 | See next page for caption.

Extended Data Fig. 5 | Sleep fragmentation does not activate the peripheral sympathetic nervous system but has effects on hypothalamic gene transcription and food consumption. a, Plasma corticosterone levels in *Apoe*$^{-/-}$ mice and *Apoe*$^{-/-}$ mice after 16 weeks of sleep fragmentation at ZT3 and ZT14 ($n = 4$ mice per group, except $n = 5$ *Apoe*$^{-/-}$ mice at ZT3). **b**, Systolic and diastolic blood pressure at ZT3 ($n = 4$ mice per group). **c**, Immunohistochemical analysis and quantification of tyrosine hydroxylaze (TH) staining in the bone marrow of *Apoe*$^{-/-}$ mice, *Apoe*$^{-/-}$ SF mice and *Apoe*$^{-/-}$ mice subjected to 3 weeks of chronic variable stress ($n = 4$ *Apoe*$^{-/-}$ mice; $n = 4$ *Apoe*$^{-/-}$ SF mice; $n = 3$ *Apoe*$^{-/-}$ stressed mice). **d**, Quantification at ZT3 of blood Ly-6C^{high} monocytes and neutrophils, bone marrow LSK cells and proliferation in *Apoe*$^{-/-}$ mice and *Apoe*$^{-/-}$ SF mice after antagonism of the β3 receptor for 4 weeks ($n = 3$ *Apoe*$^{-/-}$ mice treated with β3 blocker; $n = 4$ *Apoe*$^{-/-}$ SF mice treated with β3 blocker). **e**, Quantification of time in outer zone during open field test ($n = 9$ *Apoe*$^{-/-}$ mice; $n = 8$ *Apoe*$^{-/-}$ SF mice). **f**, Quantification of time spent in light box during light–dark box test ($n = 6$ per group). **g**, Quantification of time in new arm during Y-maze test ($n = 8$ *Apoe*$^{-/-}$ mice; $n = 5$ *Apoe*$^{-/-}$ SF mice). **h**, Analysis of neuropeptide expression in the hypothalamus at ZT3 ($n = 5$ *Apoe*$^{-/-}$ mice, except $n = 6$ for *Pmch*, *Tph2*, *Gad1*and *Npy*; $n = 5$ *Apoe*$^{-/-}$ SF mice, except $n = 4$ for *Npy*). **i**, Neuropeptide receptor expression in the hypothalamus at ZT3 ($n = 6$ *Apoe*$^{-/-}$ mice, except *Hcrtr1*, $n = 10$ mice; $n = 5$ *Apoe*$^{-/-}$ SF mice, except *Hcrtr2*, $n = 6$ mice). **j**, Circadian gene expression in the hypothalamus at ZT3 and ZT14 ($n = 3$ *Apoe*$^{-/-}$ mice; $n = 4$ *Apoe*$^{-/-}$ SF mice). **k**, Mouse food consumption during the course of sleep fragmentation ($n = 4$ *Apoe*$^{-/-}$ mice at ZT3, except $n = 6$ *Apoe*$^{-/-}$ mice on HFD for 16 weeks at ZT3; $n = 4$ *Apoe*$^{-/-}$ SF mice at ZT3, except $n = 6$ *Apoe*$^{-/-}$ SF mice on HFD for 16 weeks at ZT3; $n = 5$ *Apoe*$^{-/-}$ mice at ZT14, except $n = 4$ *Apoe*$^{-/-}$ mice on HFD for 10 weeks at ZT14 and $n = 6$ *Apoe*$^{-/-}$ mice on HFD for 16 weeks at ZT14; $n = 5$ *Apoe*$^{-/-}$ SF mice at ZT14, except $n = 4$ *Apoe*$^{-/-}$ SF mice on HFD for 10 weeks at ZT14 and $n = 6$ *Apoe*$^{-/-}$ SF mice on HFD for 16 weeks at ZT14). Data are mean ± s.e.m., $^{*}P < 0.05$, $^{**}P < 0.01$, two-tailed Mann–Whitney *U*-tests. ns, not significant.

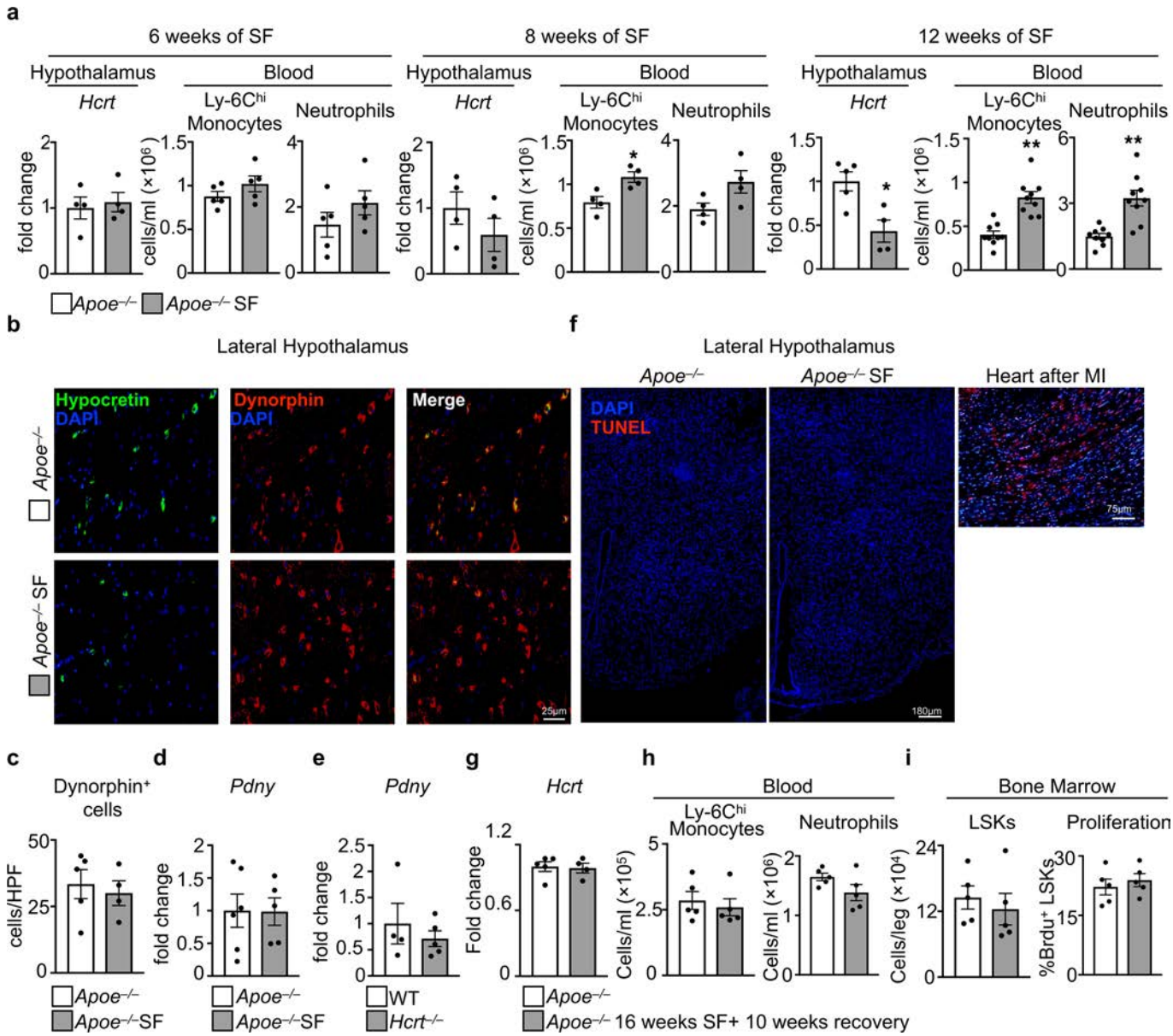

Extended Data Fig. 6 | Hypothalamic expression of hypocretin and dynorphin. a, Hypothalamic expression of hypocretin and quantification of blood Ly-6C^{high} monocytes and neutrophils in *Apoe*$^{-/-}$ mice after 6, 8 and 12 weeks of sleep fragmentation (for *Hcrt*, $n = 4$ *Apoe*$^{-/-}$ mice, except $n = 5$ for *Apoe*$^{-/-}$ mice after 12 weeks; for *Hcrt*, $n = 4$ *Apoe*$^{-/-}$ SF mice; for blood cells at 6 weeks, $n = 5$ mice per group; for blood cells at 8 weeks, $n = 4$ mice per group; for blood cells at 12 weeks, $n = 9$ mice per group). **b**, Sections of the hypothalamus stained for dynorphin and hypocretin. **c**, Quantification of hypothalamic dynorphin^{+} cells per high-powered field of view ($n = 5$ *Apoe*$^{-/-}$ mice; $n = 4$ *Apoe*$^{-/-}$ SF mice, of two independent experiments). **d**, **e**, Dynorphin (*Pdny*) mRNA expression in the hypothalamus of SF mice (**d**; $n = 6$ *Apoe*$^{-/-}$ mice; $n = 5$ *Apoe*$^{-/-}$ SF mice) and *Hcrt*$^{-/-}$ mice (**e**; $n = 4$ wild-type mice; $n = 5$ *Hcrt*$^{-/-}$ mice). **f**, TUNEL staining of hypothalamic sections from *Apoe*$^{-/-}$ and *Apoe*$^{-/-}$ SF mice (representative of four biological replicates) along with a positive control of TUNEL-stained myocardium 1 day after myocardial infarction (MI) ($n = 1$). **g–i**, *Apoe*$^{-/-}$ mice were sleep-fragmented for 16 weeks then allowed to recover and sleep normally for 10 weeks. Control mice slept normally for 26 weeks. **g**, Analysis of hypothalamic hypocretin expression ($n = 5$ *Apoe*$^{-/-}$ mice; $n = 4$ *Apoe*$^{-/-}$ SF mice). **h**, Blood Ly-6C^{high} monocytes and neutrophils ($n = 5$ mice per group). **i**, Quantification of bone marrow LSK cells and proliferation of LSK cells ($n = 5$ mice per group). Data are mean ± s.e.m., $^{*}P < 0.05$, $^{**}P < 0.01$, two-tailed Mann–Whitney *U*-tests.

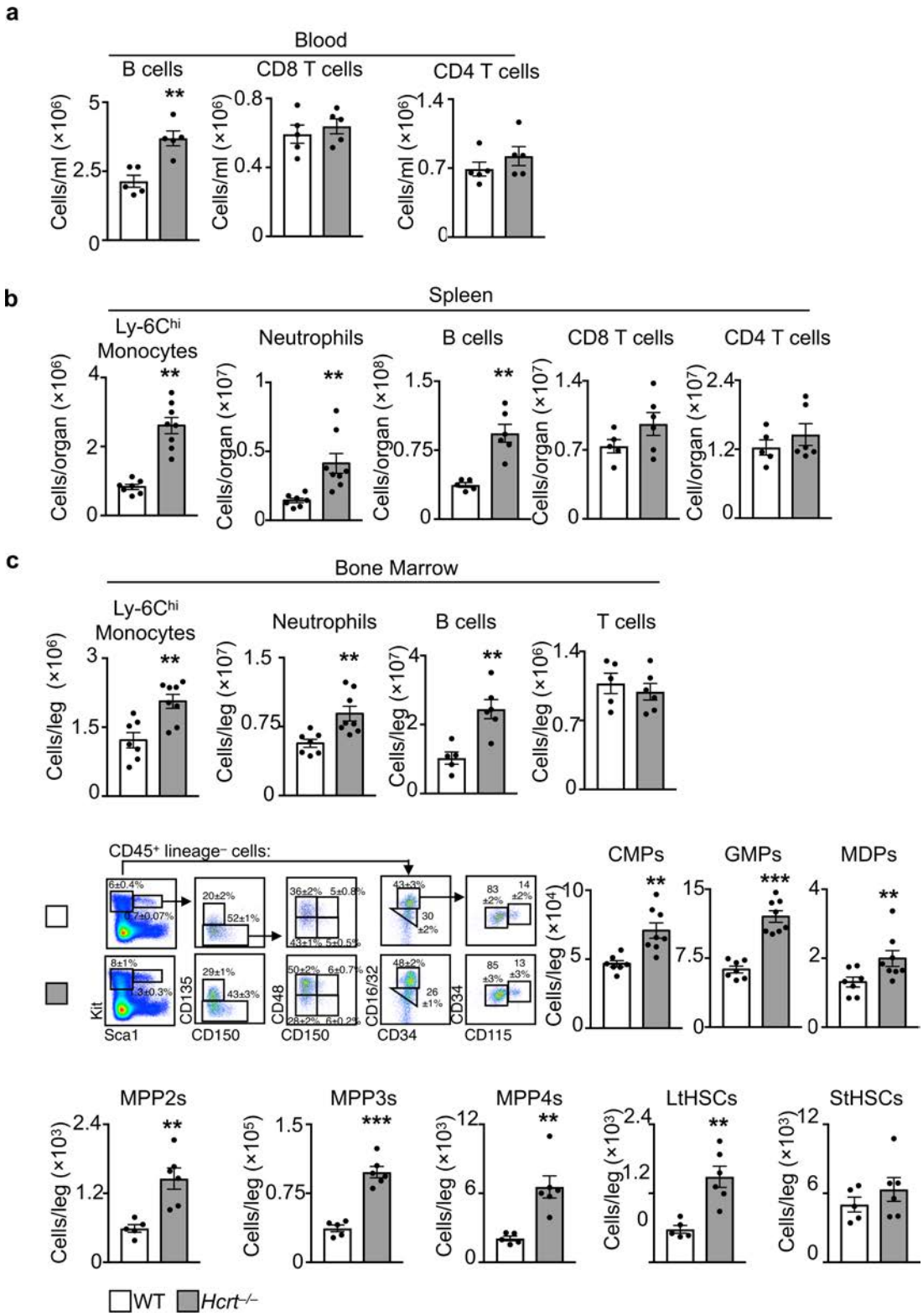

Extended Data Fig. 7 | Haematopoiesis in hypocretin-deficient mice. a–c, Quantification of the number of leukocytes in wild-type and *Hcrt*$^{-/-}$ mice at ZT3 in blood (**a**; $n = 5$ mice per group), spleen (**b**; for Ly-6C^{high} monocytes and neutrophils, $n = 7$ wild-type mice and $n = 8$ *Hcrt*$^{-/-}$ mice; for B, CD8^{+} T, and CD4^{+} T cells, $n = 5$ wild-type mice and $n = 6$ *Hcrt*$^{-/-}$ mice) and bone marrow (**c**; for Ly-6C^{high} monocytes and neutrophils, $n = 7$ wild-type mice and $n = 8$ *Hcrt*$^{-/-}$ mice; for B and T cells, $n = 5$ wild-type mice and $n = 6$ *Hcrt*$^{-/-}$ mice; for CMPs, GMPs and MDPs, $n = 7$ wild-type mice and $n = 8$ *Hcrt*$^{-/-}$ mice; for LSK populations, $n = 5$ wild-type mice and $n = 6$ *Hcrt*$^{-/-}$ mice). Data are mean ± s.e.m., $^{**}P < 0.01$, $^{***}P < 0.001$, two-tailed Mann–Whitney *U*-tests.

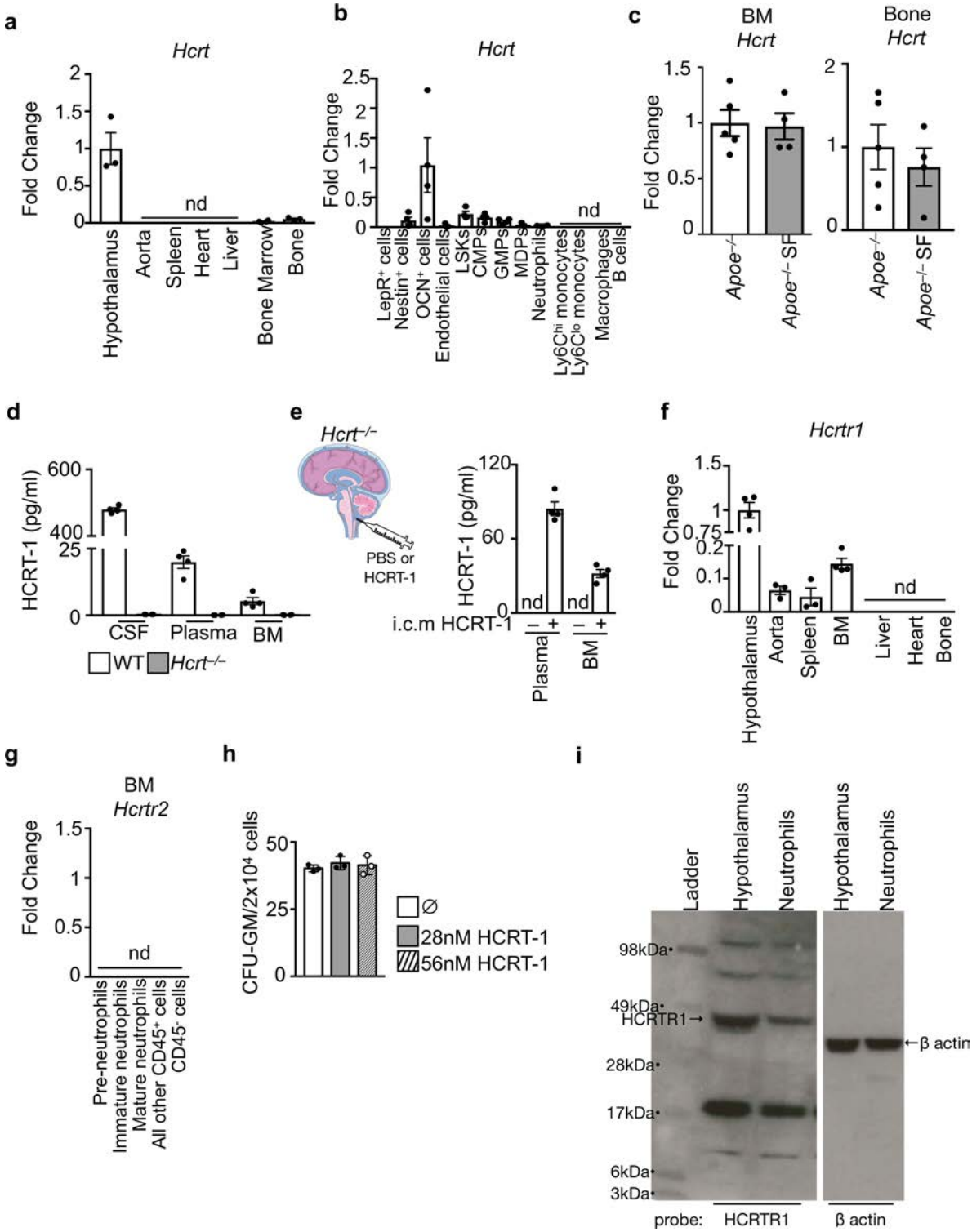

Extended Data Fig. 8 | Hypocretin and hypocretin receptor-1 expression and production. a, **b**, Relative *Hcrt* mRNA expression in tissues (**a**; $n = 3$) and sorted bone marrow cells (**b**; $n = 4$). **c**, *Hcrt* expression in the bone marrow and bone in *Apoe*$^{-/-}$ mice and in *Apoe*$^{-/-}$ mice subjected to sleep fragmentation for 16 weeks ($n = 5$ *Apoe*$^{-/-}$ mice; $n = 4$ *Apoe*$^{-/-}$ SF mice). **d**, Hypocretin-1 protein levels in cerebrospinal fluid (CSF), plasma and bone marrow (BM) fluid of wild-type and *Hcrt*$^{-/-}$ mice ($n = 4$ mice per group). **e**, Hypocretin-1 protein levels in the plasma and bone marrow fluid of *Hcrt*$^{-/-}$ mice 3 h after intra-cisterna magna (i.c.m.) injection of HCRT-1 or PBS. ($n = 4$ mice per group). **f**, Relative *Hcrtr1* mRNA expression in tissues ($n = 4$ mice, except aorta and spleen, $n = 3$). **g**, *Hcrtr2* expression in sorted bone marrow cells ($n = 4$ mice). **h**, Granulocyte–macrophage colony forming units (CFU-GM) from bone marrow cells of wild-type mice exposed to hypocretin-1 ex vivo in culture medium ($n = 3$ per group). **i**, Assessment of hypocretin receptor-1 protein in hypothalamus and sorted bone marrow neutrophils by western blot. Data are mean ± s.e.m.

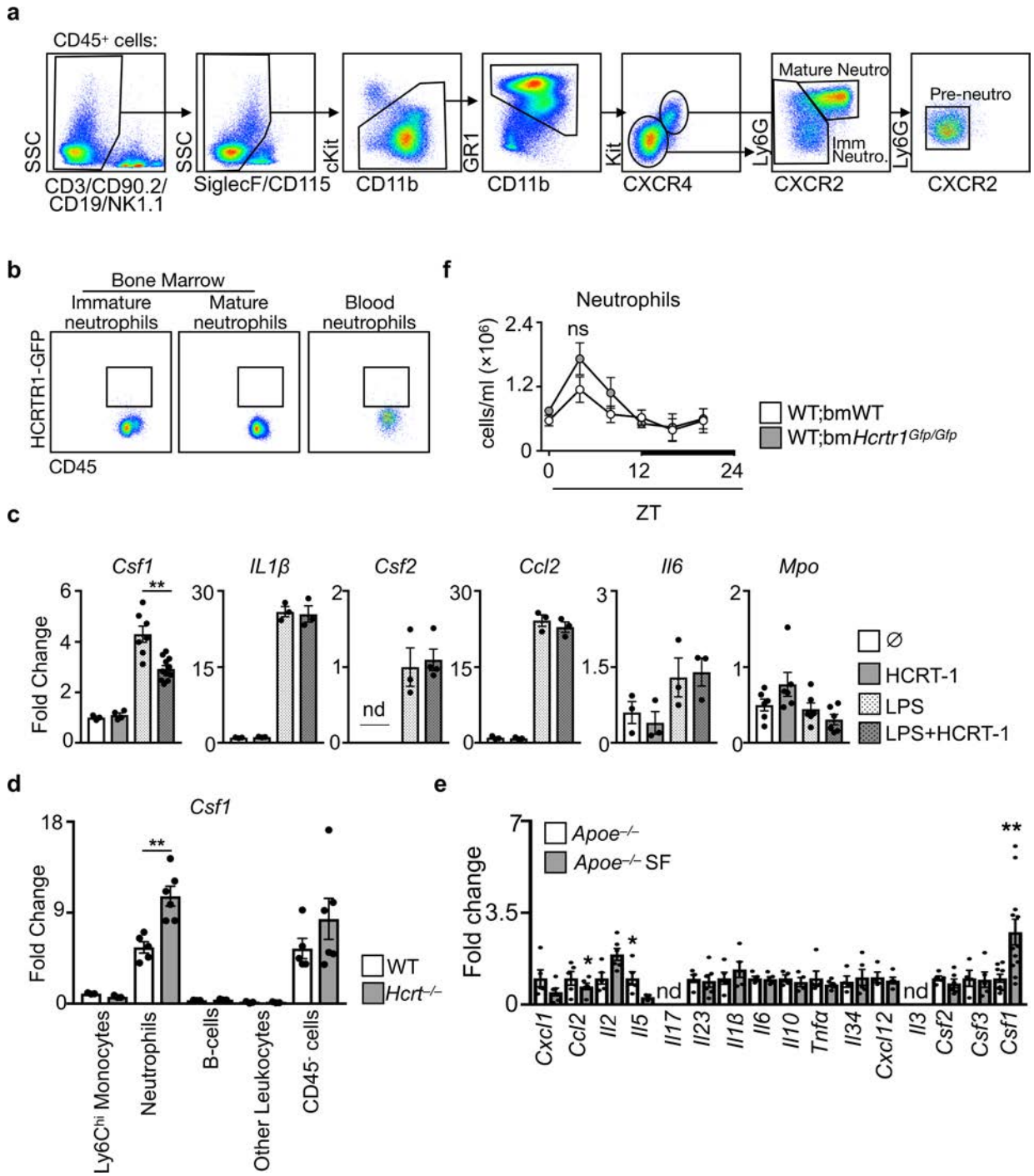

Extended Data Fig. 9 | Hypocretin, bone marrow neutrophils and HCRTR1. a, Flow cytometry gating strategy for bone marrow pre-neutrophils, immature neutrophils and mature neutrophils. **b**, HCRTR1 (GFP) in bone marrow and blood neutrophils from WT;bm*Hcrtr1*$^{GFP/GFP}$ mice. **c**, mRNA expression in cultured bone marrow pre-neutrophils exposed to LPS and/or HCRT-1 (for untreated $n = 3$ mice, except *Mpo*, $n = 6$ mice; for HCRT-1, $n = 3$ mice, expect *Csf1*, $n = 4$ mice and *Mpo*, $n = 6$ mice; for LPS, $n = 3$ mice except *Csf1*, $n = 7$ mice and *Mpo*, $n = 6$ mice; for LPS and HCRT-1, $n = 3$ mice, except *Csf1*, $n = 11$ mice, *Csf2*, $n = 4$ mice and *Mpo*, $n = 6$ mice). **d**, *Csf1* expression in sorted bone marrow cells of wild-type and *Hcrt*$^{-/-}$ mice ($n = 5$ wild-type mice; $n = 6$ *Hcrt*$^{-/-}$ mice). **e**, Analysis of mRNA transcript expression in bone marrow leukocytes of *Apoe*$^{-/-}$ mice after 16 weeks of sleep fragmentation (for *Apoe*$^{-/-}$, $n = 5$ mice, except *Il10*, *Il34*, *Cxcl12*, *Csf3*, $n = 4$ mice and *Csf1*, $n = 9$ mice; for *Apoe*$^{-/-}$ SF mice, $n = 6$ mice, except *Il5*, *Il1β*, *Il6*, *Il34*, *Cxcl12*, *Csf3*, $n = 5$, *Il10*, $n = 5$ mice and *Csf1*, $n = 12$). nd, not detected. **f**, Blood neutrophils in WT;bm*Hcrtr1*$^{GFP/GFP}$ mice over 24 h ($n = 3$ per group). Data presented as mean ± s.e.m., $^{**}P < 0.01$, one-way ANOVA.

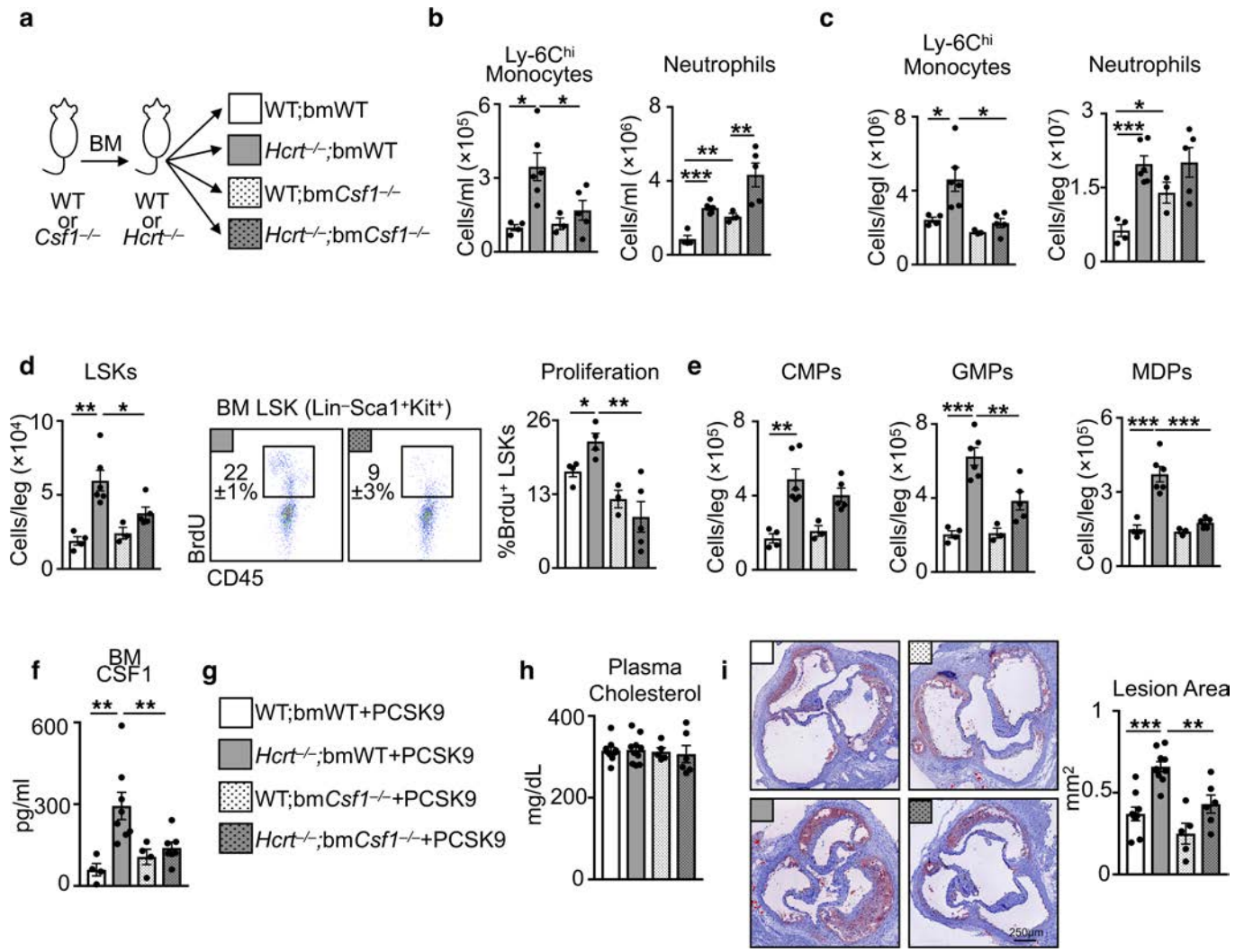

Extended Data Fig. 10 | Haematopoietic CSF1 deletion protects against haematopoiesis and atherosclerosis in hypocretin-deficient mice. **a**, Schematic of chimeric models. **b**, **c**, Quantification of Ly-6C^{high} monocytes and neutrophils in blood (**b**; $n = 4$ WT;bmWT mice; $n = 6$ *Hcrt*$^{-/-}$;bmWT mice; $n = 3$ WT;bm*Csf1*$^{-/-}$ mice; $n = 5$ *Hcrt*$^{-/-}$;bm*Csf1*$^{-/-}$ mice) and bone marrow (**c**; $n = 4$ WT;bmWT mice; $n = 6$ *Hcrt*$^{-/-}$;bmWT mice; $n = 3$ WT;bm*Csf1*$^{-/-}$ mice; $n = 5$ *Hcrt*$^{-/-}$;bm*Csf1*$^{-/-}$ mice). **d**, Quantification of the number of LSK cells ($n = 4$ WT;bmWT mice; $n = 6$ *Hcrt*$^{-/-}$;bmWT mice; $n = 3$ WT;bm*Csf1*$^{-/-}$ mice; $n = 5$ *Hcrt*$^{-/-}$;bm*Csf1*$^{-/-}$ mice) and proliferation ($n = 4$ WT;bmWT mice; $n = 4$ *Hcrt*$^{-/-}$;bmWT mice; $n = 3$ WT;bm*Csf1*$^{-/-}$ mice; $n = 5$ *Hcrt*$^{-/-}$;bm*Csf1*$^{-/-}$ mice) in bone marrow. **e**, Quantification of CMPs, GMPs and MDPs in chimeric mice ($n = 4$ WT;bmWT mice; $n = 6$ *Hcrt*$^{-/-}$;bmWT mice; $n = 3$ WT;bm*Csf1*$^{-/-}$ mice; $n = 5$ *Hcrt*$^{-/-}$;bm*Csf1*$^{-/-}$ mice). **f**, Bone marrow CSF1 levels ($n = 4$ WT;bmWT mice; $n = 8$ *Hcrt*$^{-/-}$;bmWT mice; $n = 4$ WT;bm*Csf1*$^{-/-}$ mice; $n = 7$ *Hcrt*$^{-/-}$;bm*Csf1*$^{-/-}$ mice). **g**, Schematic of chimeric models receiving Adv-PCSK9 and fed a HCD for 12 weeks. **h**, Plasma cholesterol levels ($n = 7$ WT;bmWT mice; $n = 10$ *Hcrt*$^{-/-}$;bmWT mice; $n = 5$ WT;bm*Csf1*$^{-/-}$ mice; $n = 6$ *Hcrt*$^{-/-}$;bm*Csf1*$^{-/-}$ mice). **i**, Images of cross-sections of aortic roots stained with oil red O and quantification of atherosclerosis in chimeric mice ($n = 7$ WT;bmWT mice; $n = 9$ *Hcrt*$^{-/-}$;bmWT mice; $n = 5$ WT;bm*Csf1*$^{-/-}$ mice; $n = 6$ *Hcrt*$^{-/-}$;bm*Csf1*$^{-/-}$ mice). Data are mean ± s.e.m., $^{*}P < 0.05$, $^{**}P < 0.01$, $^{***}P < 0.001$, one-way ANOVA.

nature research

Corresponding author(s): Filip Swirski

Last updated by author(s): Dec 20, 2018

Reporting Summary

Nature Research wishes to improve the reproducibility of the work that we publish. This form provides structure for consistency and transparency in reporting. For further information on Nature Research policies, see Authors & Referees and the Editorial Policy Checklist.

Statistics

For all statistical analyses, confirm that the following items are present in the figure legend, table legend, main text, or Methods section.

n/a	Confirmed	
☐	☒	The exact sample size (*n*) for each experimental group/condition, given as a discrete number and unit of measurement
☐	☒	A statement on whether measurements were taken from distinct samples or whether the same sample was measured repeatedly
☐	☒	The statistical test(s) used AND whether they are one- or two-sided *Only common tests should be described solely by name; describe more complex techniques in the Methods section.*
☐	☒	A description of all covariates tested
☐	☒	A description of any assumptions or corrections, such as tests of normality and adjustment for multiple comparisons
☐	☒	A full description of the statistical parameters including central tendency (e.g. means) or other basic estimates (e.g. regression coefficient) AND variation (e.g. standard deviation) or associated estimates of uncertainty (e.g. confidence intervals)
☒	☐	For null hypothesis testing, the test statistic (e.g. *F*, *t*, *r*) with confidence intervals, effect sizes, degrees of freedom and *P* value noted *Give P values as exact values whenever suitable.*
☒	☐	For Bayesian analysis, information on the choice of priors and Markov chain Monte Carlo settings
☒	☐	For hierarchical and complex designs, identification of the appropriate level for tests and full reporting of outcomes
☐	☒	Estimates of effect sizes (e.g. Cohen's *d*, Pearson's *r*), indicating how they were calculated

Our web collection on statistics for biologists contains articles on many of the points above.

Software and code

Policy information about availability of computer code

Data collection	BD FACSDiVa software was used to collect data from flow cytometry; NPDview2 and Nanozoomer 2.0Rs were used to collect histology data.
Data analysis	Flow cytometric analyses were performed with FlowJo software (FlowJo 8.7.2); NPDviewview2 software was used to analyze histology data; Statistical analyses were performed with GraphPad Prism 7.0 software

For manuscripts utilizing custom algorithms or software that are central to the research but not yet described in published literature, software must be made available to editors/reviewers. We strongly encourage code deposition in a community repository (e.g. GitHub). See the Nature Research guidelines for submitting code & software for further information.

Data

Policy information about availability of data

All manuscripts must include a data availability statement. This statement should provide the following information, where applicable:

- Accession codes, unique identifiers, or web links for publicly available datasets
- A list of figures that have associated raw data
- A description of any restrictions on data availability

The authors declare that all data supporting the findings of this study are available within the paper and its supplementary information files.

Field-specific reporting

Please select the one below that is the best fit for your research. If you are not sure, read the appropriate sections before making your selection.

☒ Life sciences ☐ Behavioural & social sciences ☐ Ecological, evolutionary & environmental sciences

Life sciences study design

All studies must disclose on these points even when the disclosure is negative.

Sample size	Power calculations were performed to determine sample size.
Data exclusions	No data were excluded from analysis.
Replication	All attempts at replication were successful. Findings were replicated in at least three biologically independent samples each.
Randomization	WHere appropriate, the mice were selected at random. Otherwise, animals were placed into separate groups according to their genotype.
Blinding	Where possible, groups were blinded

Reporting for specific materials, systems and methods

We require information from authors about some types of materials, experimental systems and methods used in many studies. Here, indicate whether each material, system or method listed is relevant to your study. If you are not sure if a list item applies to your research, read the appropriate section before selecting a response.

Materials & experimental systems

n/a	Involved in the study
☐	☒ Antibodies
☒	☐ Eukaryotic cell lines
☒	☐ Palaeontology
☐	☒ Animals and other organisms
☒	☐ Human research participants
☒	☐ Clinical data

Methods

n/a	Involved in the study
☒	☐ ChIP-seq
☐	☒ Flow cytometry
☒	☐ MRI-based neuroimaging

Antibodies

Antibodies used	anti-CD45 (BioLegend, clone30-F11, Cat#103147, Lot#B243834), anti-CD45.1 (BioLegend, clone A20, Cat#110708), anti-CD45.2 (BioLegend, clone 104, Cat#109802), anti-CD3 (BioLegend, clone 17A2, Cat#100206), anti-CD90.2 (BioLegend, clone 53-2.1, Cat#105308, Lot#B260050), anti-CD19 (BioLegend, clone 6D5, Cat#115508, Lot#B226581), anti-B220 (BD Biosciences, clone RA3-6B2, Cat#553089, Lot#6012954), anti-NK1.1 BioLegend, clone PK136, Cat#108708), anti-Ly6G (BioLegend, clone 1A8, Cat127614#, Lot#B259670), anti-Ly6C (BioLegend, AL-21, Cat#128006, Lot#B247728), anti-MHCII (BioLegend, clone M5/114.152, Cat#107602, Lot#B217859), anti-F4/80 (Biolegend, clone BM8, Cat#123114, Lot#B237342), anti-CD11b (BioLegend, clone M1/70, Cat#101226, Lot#B238268), anti-CD115 (BioLegend, clone AFS98, Cat#135517, Lot#B265220), anti-Ter119 (BioLegend, clone TER-119, Cat#116208, Lot#B220899), anti-CD34 (eBioscience, clone RAM34, Cat#11-0341-85, Lot#E00265-1634), anti-CD49b (BioLegend, clone DX5, Cat#1089008, Lot#B258302), ant-CD11c (BioLegend, clone N418, Cat#117310, Lot#B206713), anti-IL7Rα (BioLegend, clone SB/199, Cat#121112, Lot#B189668), anti-CD16/32 (BioLegend, clone 93, Cat#101324, Lot#B250025), anti-CD150 (BioLegend, clone TC15-12F12.2, Cat#115922, Lot#B220585), anti-cKit (BioLegend, clone 2B8, Cat#105814, Lot#B252918), anti-CD135 (BioLegend, clone A2F10, Cat#135310, Lot#B234045), anti-CD48 (BioLegend, clone HM48-1, Cat#103426, Lot#B236445), anti-Sca1 (BioLegend, clone D7, Cat#108126, Lot#B234288), anti-CD8 (BD Bioscience, clone 53-6.7, Cat#553035, Lot#2296946), anti-CD4 (BioLegend, clone GK1.5, Cat#100428, Lot#B237336), anti-SiglecF (BD Pharmingen, clone E50-2440, Cat#562680, Lot#7054789), anti-CXCR4 (Invitrogen, clone 2B11, Cat#12-9991-81, Lot#B251481), anti-CXCR2 (BioLegend, clone SA044G4, Cat#149307, Lot#B251481), anti-BrdU (eBioscience, clone BU20A, Cat#17-5071-42, Lot#4319920). All antibodies were used in a 1:700 dilution.
Validation	These antibodies were all used for flow cytometry on mice. Antibody validations were performed by antibody suppliers per quality assurance literature provided by each supplier.

Animals and other organisms

Policy information about studies involving animals; ARRIVE guidelines recommended for reporting animal research

Laboratory animals	C57BL/6J (wild type, WT), Apoetm1Unc (Apoe−/−), Ldlrtm1Her/J (Ldlr−/−) and Csf1op (Csf1−/−) mice were purchased from The Jackson Laboratory (Bar Harbor, ME, USA). Hcrt−/− mice were kindly provided by Dr. Thomas Scammell (Professor of Neurology, Division of Sleep Science, Harvard Medical School) and bred in-house. HcrtR1GFP/GFP mice were kindly provided by Dr. Anne Vassalli (Department of Physiology, University of Lausanne). Stromal cell reporter mice Nestin-GFP, LeptinRcre-R26-EYFP, and OCN-GFPtopaz− were bred in-house. Age- and sex-matched animals were used at 8–12 weeks of age. For experiments on Apoe-/- and Ldlr-/- mice females were used. In all other experiments both males and females were used.

Wild animals	This study did not involve wild animals
Field-collected samples	This study did not involve samples collected from the field.
Ethics oversight	All protocols were approved by the Animal Review Committee at the Massachusetts General Hospital

Note that full information on the approval of the study protocol must also be provided in the manuscript.

Flow Cytometry

Plots

Confirm that:

☐ The axis labels state the marker and fluorochrome used (e.g. CD4-FITC).

☐ The axis scales are clearly visible. Include numbers along axes only for bottom left plot of group (a 'group' is an analysis of identical markers).

☐ All plots are contour plots with outliers or pseudocolor plots.

☒ A numerical value for number of cells or percentage (with statistics) is provided.

Methodology

Sample preparation	Peripheral blood was collected by retro-orbital bleeding and red blood cells were lysed in RBC lysis buffer (Biolegend, San Diego, CA). Aortas, lung, liver and heart were excised after PBS (Thermo Fisher Scientific, Waltham, MA) perfusion, minced and digested with 450 U/ml collagenase I, 125 U/ml collagenase XI, 60 U/ml DNase I and 60 U/ml hyaluronidase (Sigma-Aldrich, St. Louis, MO) in PBS for 20 minutes (liver), 40 minutes (aorta) or 1hr (heart and lung) at 37°C. Spleens were crushed through a 40mm cell strained and red blood cells were lysed with RBC lysis buffer. Bone marrow cells were collected by flushing bones with PBS after which a single cell suspension was created by passing cells through a 26-gage needle and red blood cells were lysed with RBC lysis buffer.
Instrument	Data were acquired on a LSRII and a Area II
Software	DIVA and FlowJo
Cell population abundance	Post sort, cell abundance was sufficient for down stream applications. After sorting, a small fraction of the sorted cells were run through Aria II and the same gating strategy was applied to check the purity of sorted cell populations. A general purity of higher than 95% were achieved for all the sorted population.
Gating strategy	FSC/SSC gating was used to exclude dead cells and debris followed by FSCA/FSCH to select singlets. Viable cells were identified as unstained with Zombie Aqua (Biolegend, CA). Cells were identified as (i) Ly6Chigh monocytes (CD45+Lin1–CD11b+CD115+F4/80–Ly-6Chigh), (ii) neutrophils (CD45+Lin1–CD11b+Ly-6G+F4/80–), (iii) macrophages (CD45+Lin1–CD11b+F4/80+Ly-6Clow), (iv) B-cells (CD45+B220+CD19+F4/80–CD11b–), (v) CD4 T-cells (CD45+CD3+CD90+CD4+CD11b–F4/80–), (vi) CD8 T-cells (CD45+CD3+CD90+CD8+CD11b–F4/80–), (vii) LSKs (CD45+Lin2–cKit+Sca1+), (viii) MPP4 (CD45+Lin2–cKit+Sca1+CD135+CD150–), (ix) MPP3 (CD45+Lin2–cKit+Sca1+CD135+CD150–CD48+), (x) MPP2 (CD45+Lin2–cKit+Sca1+CD135+CD150+CD48+), (xi) short-term hematopoietic stem cell (StHSC, CD45+Lin2–cKit+Sca1+CD135+CD150–CD48-), (xii) LtHSC (CD45+Lin2–cKit+Sca1+CD135+CD150+CD48-), (xiii) common myeloid progenitor (CMP, CD45+Lin2–cKit+Sca1–CD34+CD16/32mid), (xiv) granulocyte/macrophage progenitor (GMP, CD45+Lin2–cKit+Sca1–CD34+CD16/32highCD115–), (xv) monocyte-dendritic cell progenitor (MDP, CD45+Lin2–cKit+Sca1–CD34+CD16/32highCD115+), for neutrophils populations (CD45+CD3-CD90.2-CD19-NK1.1-SiglecF-CD115-cKitlowCD11b+Gr-1+) (xvi) pre-neutrophils were then separated as cKitintCXCR4+CXCR2-, (xvii) immature neutrophils as ckit-CXCR4-CXCR2-, and (xviii) mature neutrophils as ckit-CXCR4-CXCR2+Ly6G+. Lineages were defined as Lin1: CD3, CD90.2, CD19, NK1.1, Ter119 and Lin2: B220, CD19, CD49b, Ter119, CD90.2, CD11b, CD11c, Ly-6G, IL7Rα. Osteolineage cells (OCN+) cells were identified as CD45–Ter119–CD31–GFP+ from the bone fraction of OCN-GFP mice. Leptin receptor (LepR+) cells were identified as CD45–Ter119–CD31–YFP+ form the bone marrow fraction of LeptinRcre-R26-EYFP. Nestin+ cells were identified as CD45–Ter119–CD31–GFP+ form the bone and bone marrow fraction of Nestin-GFP mice. Endothelial cells were identified as CD45–Ter119–CD31+ of the bone marrow fraction of LeptinRcre-R26-EYFP mice.

☒ Tick this box to confirm that a figure exemplifying the gating strategy is provided in the Supplementary Information.